



Aalto-yliopisto  
Insinöörیتieteiden  
korkeakoulu

Joakim Heinolainen

## **On the Use of Computational Fluid Dynamics for the Prediction of Wake Field in Ship Design**

Submitted as master's thesis for examination for the degree of Master of Science (Technology).

Espoo 31.12.2020

Supervisor: Professor of Practice Pekka Ruponen

Advisors: D.Sc. (Tech) Tommi Mikkola

D.Sc. (Tech) Seppo Kalske

---

**Tekijä** Joakim Heinolainen

---

**Työn nimi** Laskennallisen virtausdynamiikan käyttö vanaveden ennustamisessa laiva-suunnittelussa

---

**Maisteriohjelma** Konetekniikan maisteriohjelma **Koodi** ENG25

---

**Työn valvoja** Työelämäprofessori Pekka Ruponen

---

**Työn ohjaaja(t)** TkT Tommi Mikkola ja TkT Seppo Kalske

---

**Päivämäärä** 31.12.2020 **Sivumäärä** 60+11 **Kieli** Englanti

---

### Tiivistelmä

Energiatehokkuuden merkitys laivojen suunnittelussa on viime aikoina kasvanut johtuen päästörajoituksista ja ilmastonmuutokseen liittyvistä uhkakuvista. Olennainen osa aluksen energiatehokasta suunnittelua on kulkuvastuksen minimointi, johon voidaan vaikuttaa merkittävästi runkomuotoa optimoimalla. Aluksen energiatehokkuutta voidaan kasvattaa optimoimalla aluksen rungon muoto siten, että potkurille tulevan virtauksen laatua parannetaan. Potkuri operoi aluksen vanavedessä, joten vanaveden laadun arvioiminen on tärkeää. Vanavettä on perinteisesti tutkittu mallikokeilla mutta viime vuosikymmenten aikana laskennallisen virtausdynamiikan (CFD) avulla saaduista tuloksista on tullut riittävän tarkkoja runkomuodon optimointia varten. Jotta tuloksien perusteella voitaisiin tehdä oikeita johtopäätöksiä runkomuodon suunnittelua varten, tulee käytettyjen mallien kuvata vanaveden yksityiskohtia riittävän tarkasti.

Tämä diplomityö tarkastelee VLCC-tankkerin vanavettä hyödyntäen laskennallista virtausdynamiikkaa. Simulaatiot suoritettiin laskennallisen virtausdynamiikan ohjelmistolla Star-CCM+. Tutkittu runkomalli oli "Korean Very Large Crude Carrier 2" (KVLCC2), tutkimuskäyttöön tehty malli, jota on tutkittu laajasti muun muassa CFD-työpajoissa. Simuloinnit tehtiin mallimittakaavassa käsittelemättä vapaata nestepintaa. Virtausta mallinnettiin Reynolds-keskiarvoistetuilla Navier-Stokes -yhtälöillä ja virtaus ratkaistiin seinämälle asti käyttämättä seinämäfunktioita.

Työssä tehtiin kaksi tutkimusta. Ensiksi, hilatihennyksen vaikutusta tuloksiin tutkittiin kaarevuuskorjatulla epälinearisella turbulenssimallilla. Tutkittujen verkkojen koot olivat 0.9 miljoonasta 15.2 miljoonaan laskentatilavuutta. Lisäksi kolmea erilaista versiota SST  $k-\omega$  -turbulenssimalleista vertailtiin 7.4 miljoonan laskentatilavuuden verkolla.

Tutkimuksen tuloksia vertailtiin mallikokeista saatuihin mittaustuloksiin ja aiemmin julkaistuihin CFD-simulointien tuloksiin. Saadut tulokset olivat pääasiassa linjassa vastaavilla turbulenssimalleilla ja hilako'oilla saatujen tulosten kanssa. Huomattiin, että kaarevuuskorjattu turbulenssimalli parantaa vanaveden ennustettavuutta mallimittakaavassa. Lisäksi huomattiin, että valitun turbulenssimallin SST  $k-\omega$ :n tarkkuus ratkaistaessa seinämän lähivirtausta vaikuttaa riippuvan olennaisesti runkoa vasten olevien laskentapisteen dimensiottomasta etäisyydestä runkoon. Pienentämällä lähimpien laskentapisteen dimensiottomasta etäisyyttä rungosta ( $y^+$ ) alle nykyisten suositusten ( $y^+ \sim 1$ ), on mahdollista, että SST  $k-\omega$  -turbulenssimallin tarkkuutta voidaan parantaa merkittävästi.

---

**Avainsanat** CFD, Hydrodynamiikka, Turbulenssin mallinnus, Vanavesi, Star-CCM+

---

---

**Author** Joakim Heinolainen

---

**Title of thesis** On the Use of Computational Fluid Dynamics for the Prediction of Wake Field in Ship Design

---

**Master programme** Mechanical Engineering**Code** ENG25

---

**Thesis supervisor** Professor of Practice Pekka Ruponen

---

**Thesis advisor(s)** D.Sc. (Tech) Tommi Mikkola and D.Sc. (Tech) Seppo Kalske

---

**Date** 31.12.2020**Number of pages** 60+11**Language** English

---

**Abstract**

Energy efficiency in ship design has recently become more relevant due to emission regulations and threats regarding climate change. Essential part of energy efficient ship design is minimizing of resistance, for which optimization of hull form can affect greatly. Resistance of a ship can be minimized by optimizing hull form in such manner that improves quality of the flow to the propeller. The propeller operates in wake of the ship, and for this reason, assessing wake field quality is of high importance. Traditionally, wake field has been studied by conducting towing tank tests. During past decades, results achieved by computational fluid dynamics (CFD) have become accurate enough to be used for hull form optimization. In order to make right conclusions from the results and to use this information in design effectively, the used models must have sufficient accuracy in predicting of wake field details.

This thesis studies wake field of a VLCC-tanker by the means of computational fluid dynamics. The simulations were conducted using computational fluid dynamics software Star-CCM+. The studied hull model was Korean Very Large Crude Carrier 2 (KVLCC2), a test case model that has been widely studied for instance in CFD workshops. Simulations were conducted in model scale and without a free surface. The flow was modelled using Reynolds-Averaged Navier-Stokes equations and near wall flow was solved.

Two studies were conducted. First, a grid refinement study was conducted with curvature corrected nonlinear turbulence model. The studied mesh sizes varied from 0.9 million to 15.2 million cells. Then three different versions of SST  $k-\omega$  turbulence models were studied with a mesh consisting of 7.4 million cells.

The results were compared with towing tank tests and results from previously published CFD simulations. The results were mainly in line with the ones achieved using similar turbulence models and number of cells. It was noticed that compared to standard SST  $k-\omega$ , curvature corrected turbulence model predicts wake field more accurately in model scale. In addition, it was noticed that the accuracy of SST  $k-\omega$  turbulence model in solving of near wall flow seems to be noticeably dependent on nondimensional height of cell layer closest to the hull. By reducing the nondimensional distance of closest calculation points from the hull ( $y^+$ ) below the current recommendations ( $y^+ \sim 1$ ), it is possible that the accuracy of SST  $k-\omega$  turbulence model can be noticeably improved.

---

**Keywords** CFD, Hydrodynamics, Turbulence modelling, Wake field, Star-CCM+

---

## Acknowledgements

*First, I would like to thank my supervisor Professor Pekka Ruponen and my instructors D.Sc. (Tech) Tommi Mikkola and D.Sc. (Tech) Seppo Kalske. Their expertise and guidance provided to be very valuable. Thank you for Antti Pösö for especially practical guidance provided.*

*I would like to thank NAPA Ltd. for the equipment and premises provided for writing of the thesis.*

*Great thanks for financial support go to Foundation for Aalto University Science and Technology and Merenkulun säätiö.*

*I would like to thank Colin More for the assistance with linguistics.*

*I acknowledge the computational resources provided by the Aalto Science-IT project. Without the possibility of using them, conducting research would have been way more tedious.*

*I would like to thank my family, girlfriend and friends for their support during the thesis process. Big thanks go to Guild of Mechanical Engineering and Shipbuilders' Club for enlightening the years at university.*

*Last, I would like to thank Finnish education system for these 16 years of studying.*

*Otaniemi 31.12.2020*



*Joakim Heinolainen*

## Table of Contents

Tiivistelmä	
Abstract	
Alkusanat	
Table of Contents .....	5
Nomenclature .....	6
1 Introduction .....	8
2 Background .....	10
2.1 Energy Efficiency in Ship Design.....	10
2.2 Hull Form in Design Spiral.....	11
2.3 Computational Fluid Dynamics in Ship Design .....	13
3 Viscous Flow to Propeller Plane .....	14
3.1 Governing Equations.....	14
3.2 Flow Around Hull .....	16
3.3 Boundary Layer.....	18
3.4 Wake Field.....	20
3.5 Methods for Wake Quality Assessment .....	24
4 Applied Methods .....	26
4.1 Grid Generation.....	26
4.2 Turbulence Modeling .....	27
4.3 Discretization Methods.....	29
5 Simulation Set-Up .....	30
5.1 Case study .....	30
5.2 Computational grids .....	32
5.3 Workflow.....	37
6 Results and Discussion .....	38
6.1 Grid sensitivity study.....	38
6.2 Turbulence model comparison.....	43
6.3 Discussion.....	50
7 Conclusions .....	55
The List of Appendices .....	60
Appendices	

## Nomenclature

### Latin Alphabet

$B$	[m]	Breadth
$c_B$		Block coefficient
$C_f$		Frictional resistance coefficient
$Fn$		Froude number
$g$	[m/s <sup>2</sup> ]	Gravity
$k$	[m <sup>2</sup> /s <sup>2</sup> ]	Turbulence kinetic energy
$KG$	[m]	Vertical center of gravity
$l$	[m]	Underwater length of the hull
$L$	[m]	Length
$L_{pp}$	[m]	Length between perpendiculars
$p$	[Pa]	Pressure
$q_f$		Cell growth ratio (finer mesh)
$q_c$		Cell growth ratio (coarser mesh)
$r$		Refinement factor
$R$	[m]	Radius
$Re$		Reynolds number
$Re_L$		Local Reynolds number
$u, v, w$	[m/s]	Flow velocity in x, y and z-directions respectively
$u_\tau$	[m/s]	Friction velocity
$S$	[m <sup>2</sup> ]	Wetted surface area
$T$	[m]	Draft
$U$	[m/s]	Free stream velocity
$V_x$		Axial nondimensional velocity component
$V_r$		Radial nondimensional velocity component
$V_t$		Tangential nondimensional velocity component
$v_x$	[m/s]	Axial velocity component
$v_r$	[m/s]	Radial velocity component
$v_t$	[m/s]	Tangential velocity component
$w_F$		Froude's wake fraction
$w_n$		Nominal wake fraction
$w_p$		Potential wake fraction
$w_T$		Taylor's wake fraction
$w_v$		Viscous wake fraction
$w_w$		Wave-induced wake fraction
$y$	[m]	Wall distance
$y^+$		Nondimensional wall distance
$y_2^+$		Near-wall cell size

### Greek Symbols

$\Delta$	[m <sup>3</sup> ]	Displacement
		Change in value
$\delta$	[m]	Boundary layer thickness

$\mu$	[Pa·s]	Dynamic viscosity
$\mu_{\text{eff}}$	[Pa·s]	Effective (dynamic) viscosity
$\mu_t$	[Pa·s]	Turbulent (dynamic) viscosity
$\nu$	[m <sup>2</sup> /s]	Kinematic viscosity
$\rho$	[kg/m <sup>3</sup> ]	Density
$\sigma$	[Pa]	Stress
$\sigma_{yx}$	[Pa]	Shear stress (two-dimensional)
$\tau_w$	[Pa]	Wall shear stress
$\Phi$	[Deg]	(Peripheral) angle
$\omega$	[1/s]	Specific rate of turbulent dissipation

## Abbreviations

CAD	Computer Aided Design
CFD	Computational Fluid Dynamics
CO2	Carbon Dioxide
CPU	Central Processing Unit
DES	Detached Eddy Simulations
DNS	Direct Numerical Simulations
EARSM	Explicit Algebraic Reynolds Stress Model
EEDI	Energy Efficiency Design Index
IGES	Initial Graphics Exchange Specification, 3D CAD file format
IMO	International Maritime Organization
ITTC	International Towing Tank Conference
KRISO	Korean Research Institute of Ships and Ocean Engineering
KVLCC	Korean Very Large Crude Carrier, series of test case ship hulls
LES	Large Eddy Simulations
RANS	Reynolds-Averaged Navier-Stokes
RSM	Reynolds Stress Model
SST	Menter's Shear Stress Transport turbulence model
STL	3D file format for CAD software
USD	United States Dollar
VLCC	Very Large Crude Carrier

# 1 Introduction

Minimizing ship resistance is of key interest to both ship designers and owners when it comes to large cargo ships. Fuel costs contribute a significant portion of operational costs, thus making hull form design a critical task. By optimizing hull form, resistance that ship experiences while moving through fluid can be reduced, and quality of the flow arriving to the propeller increased. These changes reduce the required engine power, reducing emissions and saving fuel costs.

While cost effectiveness has historically been the main reason for minimizing fuel consumption, environmental aspects have been getting more relevant. The International Maritime Organization (IMO) recently formulated the Energy Efficiency for Design Index (EEDI), which set global, gradually tightening standards for the carbon dioxide (CO<sub>2</sub>) emissions of newly built ships.

Since the early 20th century, ship resistance has been predicted by conducting towing tank tests at model scale. During the 1990s, advances in computing capacity led computational fluid dynamics (CFD) to become a viable solution for predicting resistance. The benefits of this are obvious: a designer can easily compare hull forms in the early design stages at low costs. Today, ship resistance can be accurately estimated within hours or days using simulations based on the Reynolds-Averaged-Navier-Stokes (RANS) equations, which have become an industry standard. For instance, in 2010 Gothenburg Workshop, standard deviations in resistance prediction were less than five per cent for all the towed cases (Larsson et al., 2014).

Ship resistance can be divided into two main components: viscous resistance and wave making resistance. Out of these, viscous resistance plays major role in design cases below Froude number 0.3. For a typical tanker with Froude number below 0.2, viscous resistance makes up over 90% of total resistance (Larsson & Raven, 2010). This thesis focuses on viscous resistance and more specifically, the wake field of a large tanker vessel. Even small reductions in viscous resistance can result in significant fuel savings. In addition, test results for validating CFD-simulations for this type of vessel are publicly available. The Very Large Crude Carrier model KVLCC2 is used in this thesis.

An important consideration in predicting hydrodynamic performance is to estimate the flow leaving the ship (i.e., wake field), and more precisely the flow at the propeller plane. Enhancing the wake field quality by increasing uniformity and axial symmetry of the flow helps to reduce propeller loads and vibrations, and increases propeller efficiency, thus reducing the required propulsion power. Achieving a reliable wake field prediction is crucial, since methods for improving flow to the propeller are limited after building the ship.

Historically, wake field characteristics have been predicted by conducting towing tank and wind tunnel tests at model scale in order to measure the resulting flow. The model scale and the test speed are selected according to Froude number of the vessel, since wave formation scales with the Froude number. However, the viscous properties of water are not in practice scalable, causing the Reynold's number to vary greatly between model scale and full scale. Therefore, a wake measured from model scale tests does not represent the wake appearing at full scale. Typically, empirical methods are used in order to scale wake.

Despite the inaccuracies present in such predictions, CFD simulations are typically conducted in a similar way, modeling the ship at model scale and then scaling the results to predict full scale wake. This is convenient, since the results can be easily compared with those obtained from towing tank tests. In addition, model scale simulations are computationally lighter than full scale simulations, which become especially heavy if the water's free surface is simulated. On the other hand, the latter is less problematic in flows where waves have a minimal effect on the resulting wake, such as flows around slow speed cargo vessels. However, there is very limited data on full scale wake field measurements, which complicates validation of full-scale simulations.

Wake field CFD simulations typically utilize the RANS equations, and studies are conducted with or without free surface depending on the studied case. The flow around a ship's hull is highly turbulent. Due to the complexity and computational heaviness of directly solving such a turbulent flow, average turbulence is typically modelled instead. The details of the particular turbulence model chosen can have a substantial effect on the accuracy of the simulation's final predictions.

Two key questions for a ship designer are which turbulence model to select and how to generate a mesh for numerical calculations. This mesh must be fine enough to capture flow characteristics with sufficient accuracy, but also coarse enough to not use excessive computational resources. The aim of this thesis is to conduct a feasibility study of predicting wake field with different turbulence models, and a grid refinement study. The simulations were performed using RANS equations for solving the flow and using the SST  $k-\omega$  (Menter's Shear Stress Transport) turbulence model and its variations for turbulence modeling. Double body model and near wall flow were solved. Simulations were conducted at model scale. The results are compared to model scale tests and published simulation results. In addition to the presented results, there were attempts to simulate wake field flows at full scale. However, these attempts were not successful. Possible reasons for this may have been the models used, grid spacing and grid quality.

The rest of this thesis is structured as follows. Chapter 2 discusses the interests for ship resistance minimization followed by the use of computational fluid dynamics in hull form design. The chapter also briefly discusses the effect of tightening emission regulations on ship design, which also influences hull form design. Chapter 3 discusses the physics of viscous flow and the formation of the wake field, as well as methods for predicting a wake field. Chapters 4 and 5 introduce the methods used and the simulation setup, respectively. Chapter 6 presents the results, and Chapter 7 concludes the thesis by discussing the limitations and providing suggestions for future studies.

## 2 Background

This chapter presents an overview of ship resistance and wake field analysis in the context of design, together with a discussion of fuel saving potential. Section 2.1 presents the motivation for energy efficient design. Section 2.2 discusses ship design process and in which phases hull form design is conducted. Section 2.3 describes the usage of computational fluid dynamics in ship design.

### 2.1 Energy Efficiency in Ship Design

The costs of operating a very large crude carrier (VLCC) depend on the market situation, with the cost structure constantly fluctuating. For instance, from 2001 to 2010 charter rates for VLCCs varied from 20 000 to 90 000 USD per day, averaging at 55 000 USD (Polezhaeva et al., 2011). A VLCC consumes roughly 100 metric tons of bunker fuel per day at a speed of 15 knots. During the 2008-2009 financial crisis the price for this varied between roughly 20 000 and 65 000 USD (Hansen & Dinham-Peren, 2015). As a consequence, total operational costs also vary greatly depending on the market situation and shipping route. Regardless of the constantly fluctuating costs, it is clear that consumed fuel makes up a significant portion of the total cost structure.

Due to fuel costs, energy efficiency has been an important consideration in ship design for a long time. Recently, environmental aspects have also become more relevant. Shipping, as an industry, has a great potential to decrease emissions internationally. An important factor is that there are global standards for shipping which are set by International Maritime Organization (IMO). The international character of the regulations prevents ship owners from escaping the minimum standards, despite the flagging of convenience being a common practice in the industry. For instance, the regulations have a long history in providing safety rules for seafarers. However, the regulations did not significantly restrict emissions before the 2010s. Two recent emission regulations are the Energy Efficiency Design Index (EEDI), effective from 2013, and the Global Sulfur Cap, effective from 2020. EEDI directly considers the CO<sub>2</sub> emissions of shipping, and applies to ship types which are responsible for approximately 85% of the CO<sub>2</sub> emissions from international shipping (IMO, 2020). The EEDI goals include CO<sub>2</sub> reductions of 30% from 2025 and of 50% from 2050 onwards with respect to the average efficiency between 2000-2010 (IMO, 2011). Some ship owners have suggested even stricter measures for emission controls, and for instance Maersk aims to have reduced 60% of relative CO<sub>2</sub> by 2030 compared to 2008 baseline (Maersk, 2020).

The current emission reduction goals are ambitious compared to what has historically been done, and if implemented successfully, rapid advance in greener ship design can be expected in the coming decades. Alternative fuels are likely to be used since the targets cannot be solely achieved by more effective designs. However, some improvements do not require new technologies or inventions. For instance, more efficient hull forms can be designed, or propeller efficiency can be increased. Ships can be designed for slower speeds. Slower operational speeds can greatly reduce emissions, especially in the case of container vessels that typically run at Froude numbers above 0.2. For large tanker vessels running at speeds in range of Froude number 0.15, such as the KVLCC2 used in this thesis, slowing down does

not grant as significant a reduction in fuel consumption as it does for faster vessels, but it can be a partial solution. As seen, energy efficiency is a holistic ship design challenge.

Some of the ways for increasing hydrodynamic efficiency of the vessel are enhancing quality of the flow to the propeller or reducing losses occurring at propeller. This can be done by optimizing the hull shape to minimize separation of flow, for instance. In addition to hull form optimization, energy saving devices can be used to reduce energy losses occurring at aft part of the hull. These devices can recover energy by for example recovering rotational energy losses of the propeller or by improving wake quality (Bertram, 2012). Some of these include energy saving ducts and pre-swirl stators.

In order to design vessels with high propulsive efficiency or to include energy saving devices in design, a good understanding of the flow around the hull is needed. The shape of the stern should be designed to allow boundary layer to leave the hull smoothly and to minimize separation (Larsson & Raven, 2010). Research interest on energy saving devices has been increasing and for instance, at Tokyo Workshop 2015, simulations were conducted with a Japanese Bulk Carrier hull (JBC) fitted with an energy saving duct (Hino et al., 2021).

## ***2.2 Hull Form in Design Spiral***

Ships are designed for a mission and typically they are made to order. Therefore, each ship construction project is unique except for sister vessels. The intended mission of the ship sets requirements for main dimensions, cargo or passenger capacity, operational area, speed, and other design aspects. Other dimensions and the hull form are designed according to these requirements. The need for propulsion power is minimized by optimizing hull form. Since nearly every ship is unique, this optimization for achieving minimum resistance is a crucial part of most ship design projects.

These design projects typically use existing ships designed for similar missions as reference vessels. The reference vessel's quantities, such as its dimensions and required propulsion power, are used to make a parameter-based initial estimate of the corresponding quantities for the new design. From this point onwards, the design details start to get more accurate. The details need to be evaluated again after each change until design is finalized. This iterative process is commonly presented as a ship design spiral, introduced by Evans (1959). The iterative ship design process is presented in Figure 2.1.

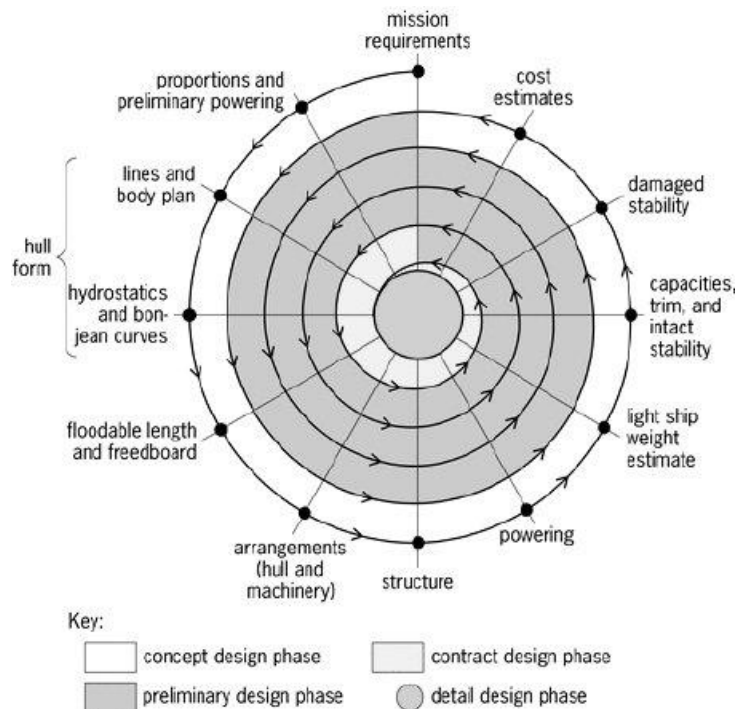


**Figure 2.1 Ship Design Spiral (Papanikolaou, 2019)**

The spiral is divided into four phases (Papanikolaou, 2019):

1. Concept design
2. Preliminary design
3. Contract design
4. Detail design

These design phases contain a vast amount of details since ships are complex structures. Here only the hydrodynamic aspects are discussed.

In the concept design phase, rough estimates of design characteristics are made based on shipowner's needs. The initial approximation is made for ship resistance and required power. This is typically based on shipyard's or designer's reference vessels and may not include simulations. In the preliminary phase, the scope of the design is narrowed down. In this phase, the hydrodynamic characteristics of the ship, such as its speed and seakeeping performance, are assessed. Model tests are typically not conducted in this design stage if hull is of a usual form (Gale, 2003). In the contract design phase, a ship specification is made to define the details and performance that the vessel should fulfill. To ensure that these will be achieved, model scale towing tank tests and additional CFD simulations are conducted. To predict propeller performance and required propulsion power, the wake field is assessed. Contract design is the most critical part of hydrodynamic design since if the ship fails to meet these requirements, the ship owner has a right to not to accept the completed ship.

Towing tank tests are expensive and time-consuming. Traditionally, hull form design has involved numerous towing tank tests, with the hull form being modified between each set of tests. Bertram (2012) mentions that occasionally this process of testing and modifying a model hull according to observations has required more than 10 iterations before satisfactory results have been achieved. Considering that towing tank tests require a vast amount of prep-

eration, and that necessary facilities typically need to be reserved well beforehand, the benefits of accurate CFD simulations are obvious. Using of CFD in early design stages can reduce total development time, reduces risks associated with the development of new vessels and can improve the outcomes of negotiations in, for example, contract design (Bertram, 2012).

Although resistance predictions from towing tank tests still tend to be more reliable than those achieved by means of CFD (Bertram, 2012), CFD can be used for comparing different hull forms and for optimizing the design accordingly. Nowadays often only the final design is validated by conducting towing tank tests (Bertram, 2012).

### **2.3 Computational Fluid Dynamics in Ship Design**

Historically, a vessel's hydrodynamic design was based on experience, and functional hull forms were copied from earlier models. The introduction of propellers as the main propulsion of vessels happened during the 19th and early 20th centuries (Carlton, 2019). Work done by Froude, Reynolds and Schoenherr (Schoenherr 1932), among others, increased our understanding of flows around ship hulls and their frictional resistance. Development of propulsion and machinery led to vessels running more efficiently and at higher operating speeds.

Bertram (2012) divides the hydrodynamic performance of a vessel into three categories: resistance and propulsion, seakeeping and ship vibrations, and maneuvering. While all of these are nowadays assessed by the means of computational fluid dynamics, only resistance and propulsion are considered here.

Towing tank tests have long been a standard procedure for measuring model scale resistance. The test results have then been corrected to full scale, typically using some of the International Towing Tank Conference (ITTC) friction lines. During the 1990s, the computational performance of computers became adequate for predicting resistance using CFD. Since then, rapid advances in computational capabilities have improved the accuracy of CFD simulations and allowed the use of more computationally heavy CFD models. For instance, Nishikawa et al. (2012) mention that the capacity of high-performance computers increased by one million times between the early 1990s and the 2010s. It is to be expected that development of this magnitude will lead to the increased use of new, computationally heavy models in the near future. Someday, CFD may even replace towing tank tests. Computational fluid dynamics could also be used for accurate full-scale resistance and wake predictions in the future.

Some of the methods for solving ship resistance related problems include potential flow codes for solving inviscid flow around the hull, double hull RANS simulations for neglecting water-air-interaction and free surface RANS simulations for taking the interaction in account. Potential flow codes can be used for predicting wave making of the vessel, double hull RANS simulations can be used for predicting friction resistance and wake of the vessel, and free surface RANS simulations can be used to predict the combined effect of wave making and frictional resistance. RANS methods are today a typical way of determining wake computationally (ITTC, 2014a). The generated mesh and chosen turbulence model have a significant impact on how accurately flow characteristics are predicted (Larsson et al., 2014).

### 3 Viscous Flow to Propeller Plane

Total ship resistance in calm water can be roughly divided into two parts: viscous resistance and wave making resistance. These parts can be assessed separately, although some interaction between them occurs. For instance, a pressure field around the hull generates waves and the boundary layer flow affects the pressure field. Since the boundary layer is thin, it is commonly assumed that the wave formation is independent of viscosity-affected boundary layer flow when predicting wave formation. (Larsson & Raven, 2010)

A more detailed way of dividing calm water resistance is given by Carlton (Carlton, 2019), in Figure 3.1.

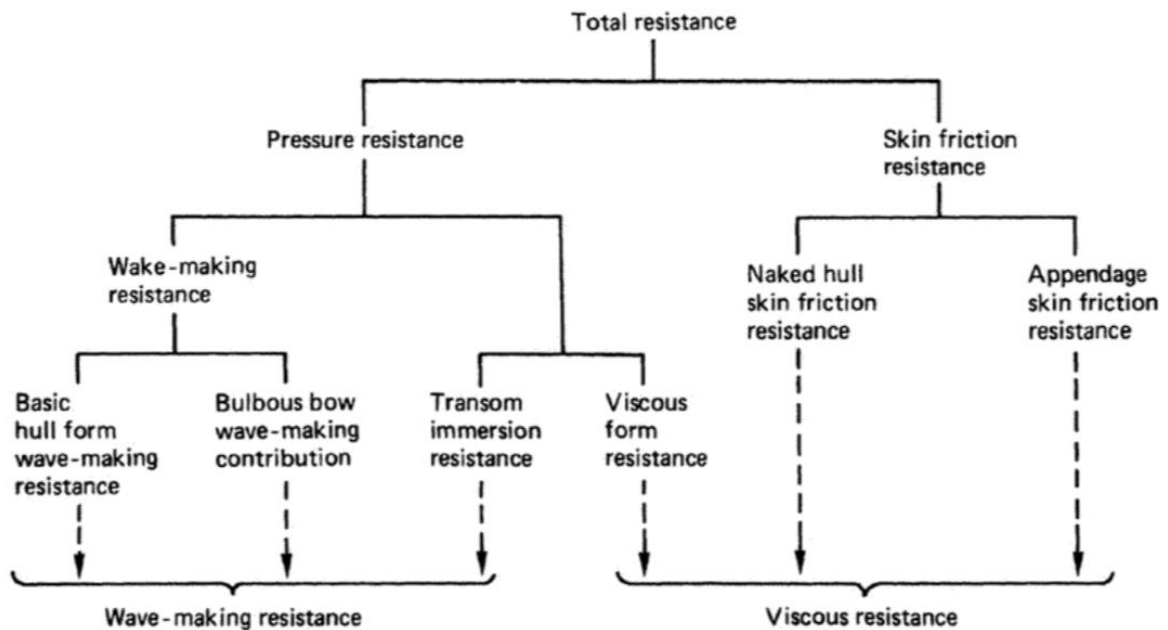


Figure 3.1 Decomposition of total resistance to friction and pressure components. (Carlton, 2019)

Here, total resistance is divided into pressure and skin friction resistance components. The viscous resistance component consists of skin friction and pressure components. Although the presented figure separates the resistance components, it should be noted that, formally, the components interact with each other as well.

Viscous flow has the largest effect on the flow arriving at the propeller. In this thesis, the wake field is assessed without the effect of a free surface, meaning that interaction between water and air is neglected. The reasoning for this is provided in Section 3.4.

#### 3.1 Governing Equations

The typical coordinate system in ship CFD assumes the vessel is in a constant position, and fluid is flowing past it at a constant velocity. The coordinate system is fixed to the vessel. In this thesis, the positive x-direction is considered to be in the direction of the vessel's velocity,

the z-axis upwards and y-axis in the port side direction. Figure 3.2 illustrates this coordinate system.



**Figure 3.2** Coordinate system.

The continuity equation for fluid applies since mass is conserved. Water is assumed to be incompressible, thus density is set to be constant. The fluid is assumed to be continuous. These assumptions simplify the continuity equation to the form for incompressible fluids, which implies that the flow rates in and out of the system are equal:

$$\frac{\partial u}{\partial x} + \frac{\partial v}{\partial y} + \frac{\partial w}{\partial z} = 0 \quad (1)$$

where  $u$  is flow velocity in the x-direction,  $v$  in the y-direction and  $w$  in the z-direction, respectively.

In order to model the physics of an incompressible flow, acceleration and three force types need to be taken into consideration: pressure forces, body forces (gravity), and viscous forces (Larsson & Raven, 2010). The resulting set of equations are called the incompressible Navier-Stokes equations. For the interested reader, the derivation is described in many pieces of literature, the book by Larsson & Raven (2010), for example.

The incompressible Navier-Stokes equations are as follows:

$$\begin{aligned} \frac{\partial u}{\partial t} + u \frac{\partial u}{\partial x} + v \frac{\partial u}{\partial y} + w \frac{\partial u}{\partial z} &= -\frac{1}{\rho} \frac{\partial p}{\partial x} + \nu \left( \frac{\partial^2 u}{\partial x^2} + \frac{\partial^2 u}{\partial y^2} + \frac{\partial^2 u}{\partial z^2} \right) \\ \frac{\partial v}{\partial t} + u \frac{\partial v}{\partial x} + v \frac{\partial v}{\partial y} + w \frac{\partial v}{\partial z} &= -\frac{1}{\rho} \frac{\partial p}{\partial y} + \nu \left( \frac{\partial^2 v}{\partial x^2} + \frac{\partial^2 v}{\partial y^2} + \frac{\partial^2 v}{\partial z^2} \right) \\ \frac{\partial w}{\partial t} + u \frac{\partial w}{\partial x} + v \frac{\partial w}{\partial y} + w \frac{\partial w}{\partial z} &= -\frac{1}{\rho} \frac{\partial p}{\partial z} - g + \nu \left( \frac{\partial^2 w}{\partial x^2} + \frac{\partial^2 w}{\partial y^2} + \frac{\partial^2 w}{\partial z^2} \right), \end{aligned} \quad (2)$$

where  $t$  denotes time,  $\rho$  denotes density,  $p$  denotes pressure,  $g$  denotes gravitational acceleration and  $\nu$  denotes kinematic viscosity.

An object moving through water accelerates the fluid particles around it. While the fluid flow far away from the object is nearly undisturbed, fluid particles close to the object are accelerated to nearly the same velocity as the object. The layers of fluid particles travelling at different velocities accelerate adjacent layers, slowing those which are faster and speeding those which are slower. In the very near proximity of the object, the velocity difference

between water molecules and the object approaches zero. This phenomenon where molecules stick to the surface is included in the model with non-slip boundary condition. This is described in more detail in next section.

### 3.2 Flow Around Hull

As previously mentioned, ship resistance in calm water can be assumed to consist of wave making resistance and viscous resistance. To explain how these components are separated from each other, the inviscid idealization and viscous flow are both discussed. First an inviscid idealization is presented.

The inviscid idealization means that fluid particles are assumed to be frictionless. An object moving through fluid forces flow to go around the object. The streamlines of fluid particles follow the hull. These changes in flow direction cause pressure variations in the flow. Pressure increases outwards from the center of curvature: high pressure points occur at the fore and aft parts of the hull, while lower pressure regions occur on the shoulders. This is illustrated in Figure 3.3.

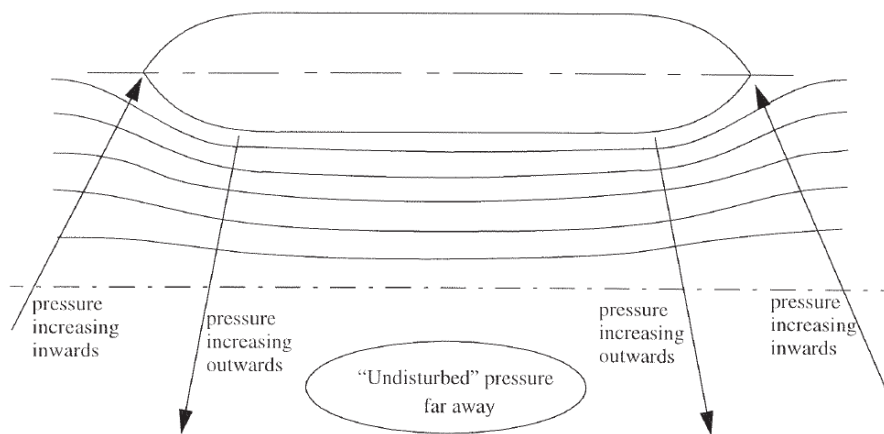


**Figure 3.3 Streamlines of inviscid flow around the hull. (Larsson & Raven, 2010)**

Excluding the water's free surface, the so-called d'Alembert's paradox applies for an object moving through fluid: when flow is considered inviscid, positive and negative pressures around an object cancel each other's out and resistance reduces to zero. This means that the resistance of the vessel consists of viscous friction induced effects on pressure when wave making is excluded.

In reality, viscosity is present in flow. In addition to causing friction resistance, this changes the pressure field around the hull. This change of pressure is what causes the form resistance, mentioned in Figure 3.1. In areas where the hull curves rapidly, increasing pressure causes the flow to slow down, which may lead to separation. This phenomenon is illustrated in Figure 3.4.

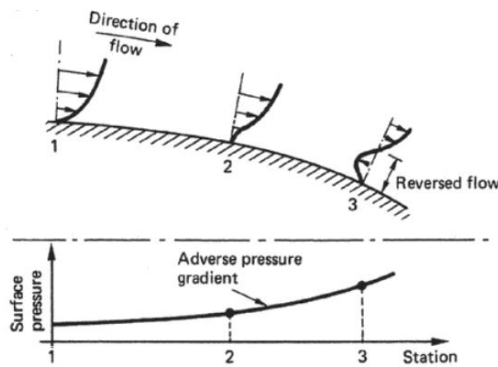


**Figure 3.4 Separation of flow (Carlton, 2019)**

In areas where streamlines converge strongly, vortex sheet separation may occur. In this event, converging streamlines force the flow to leave the surface. As a result, a strong vortex with large variations in velocity occurs, illustrated in Figure 3.5.

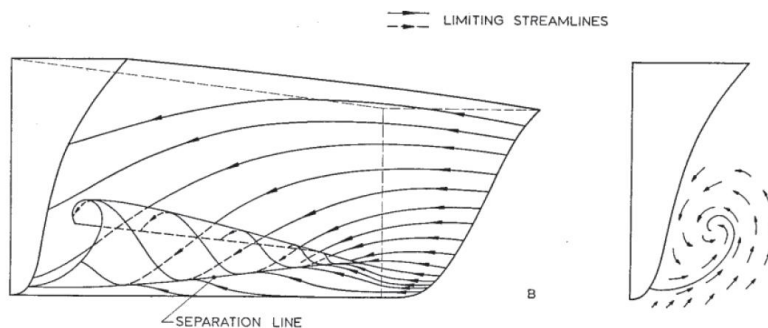


**Figure 3.5 Vortex sheet separation. (Larsson & Raven, 2010)**

The areas prone to vortex sheet separation include (Larsson & Raven, 2010):

1. On a stern bulb or the bilges in the afterbody.
2. On a barge-type stern near the bilges.
3. From a pronounced bulbous bow generating a large underpressure.
4. On a full forebody that has a deep underpressure at the fore foot.

Vortex sheet separation is a typical phenomenon in large block coefficient vessels and the phenomenon has a significant impact on resistance of the vessel, since it induces drag and changes flow to the propeller. The studied hull form KVLCC2 induces a strong bilge vortex (Kim et al., 2001).

The effects of viscous flow and separation change the pressure distribution around hull. While the pressure field around the bow remains similar to the inviscid case, the pressure is

affected more strongly towards the stern, inducing further drag on hull. These effects on the pressure field are illustrated in Figure 3.6.

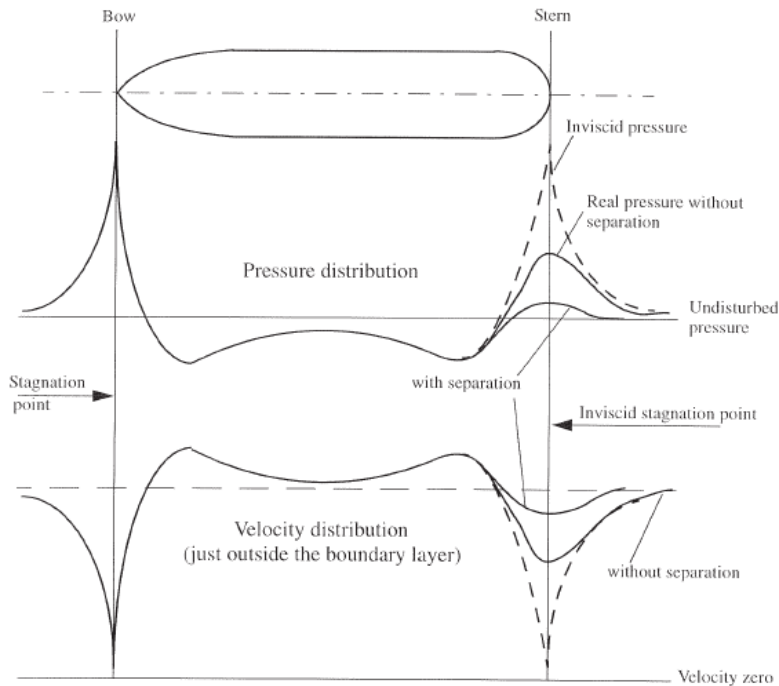


**Figure 3.6 Pressure and velocity distributions along the hull. (Larsson & Raven, 2010)**

The pressure and velocity distributions corresponding to the idealized inviscid case is indicated with a dashed line. The middle line shows the pressure distribution when separation is neglected, while the remaining line shows the behavior when separation is included to the flow.

### 3.3 Boundary Layer

Due to the viscous effects of water and interaction with the hull, water molecules stick to the hull surface, which in turn slows down the nearby flow. Similarly, faster-moving molecules transfer momentum to the slow-speed flow closer to the surface. As a result, velocity grows gradually outwards from the hull until it achieves the undisturbed flow velocity.

Flow at the very front of the hull is mostly laminar. Small instabilities in the flow grow into turbulent eddies as the fluid moves aft, and after a transition zone the boundary layer flow has become fully turbulent. This turbulent boundary layer thickens towards the aft of the hull and the size of the turbulent eddies grows, achieving diameters of the order of 1-10 meters (Larsson & Raven, 2010). If hull curvature is large, there may be separation of flow. The effect of the boundary layer flow leaving the ship is called wake and it has decreased velocity with respect to outer flow. Figure 3.7 illustrates the growth of the turbulent boundary layer. It is assumed that velocity gradients in flow are minimal outside the boundary layer. This assumption of irrotational flow means that shear stresses can be assumed to be minimal, and thus the effects of viscosity can be neglected.

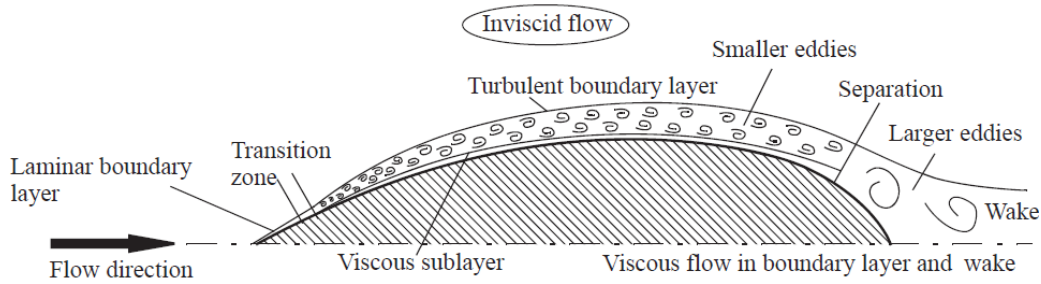


**Figure 3.7 Growth of turbulent boundary layer. (Larsson & Raven, 2010)**

Characteristics of the boundary layer depend on the amount of turbulence in the flow. Turbulent characteristics of the flow are represented by the Reynolds number, which is defined as the ratio between the inertial and viscous forces (Kundu & Cohen, 2008):

$$Re = \frac{\text{Inertia force}}{\text{Viscous force}} = \frac{Ul}{\nu}, \quad (3)$$

where  $Re$  denotes Reynolds number,  $U$  is flow (or vessel) velocity,  $l$  underwater length of the hull and  $\nu$  kinematic viscosity of the fluid. The definition of the Reynolds number tells us that turbulence in the flow increases along the hull in the direction of the flow, as seen in Figure 3.6.

The equation for shear stress in a simplified form for 2-dimensional flow can be written (Larsson & Raven, 2010) as follows:

$$\sigma_{yx} = \mu \frac{\partial u}{\partial y}, \quad (4)$$

where  $\sigma_{yx}$  is shear stress on a flat plate,  $\mu$  is dynamic viscosity,  $u$  is flow in x-direction and  $y$  is distance normal to the surface.

In practice, a nondimensional distance from the wall,  $y^+$ , is typically used within the boundary layer. It is defined as (Larsson & Raven, 2010):

$$y^+ = \frac{yu_\tau}{\nu}, \quad (5)$$

where  $u_\tau$  is friction velocity defined as:

$$u_\tau = \sqrt{\frac{\tau_w}{\rho}}, \quad (6)$$

where  $\tau_w$  is shear stress at the wall.

In different regions of the turbulent layer, viscous forces have different impacts on flow behavior due to the different velocities present. In near proximity to the hull, viscosity dominates while further from the hull, velocity of the fluid particles has larger impact on flow

behavior. Therefore, the nondimensional wall distance  $y^+$  describes local flow characteristics close to the hull. Figure 3.8 illustrates the turbulent boundary layer regions related to nondimensional wall distance in two-dimensional boundary layer flow.

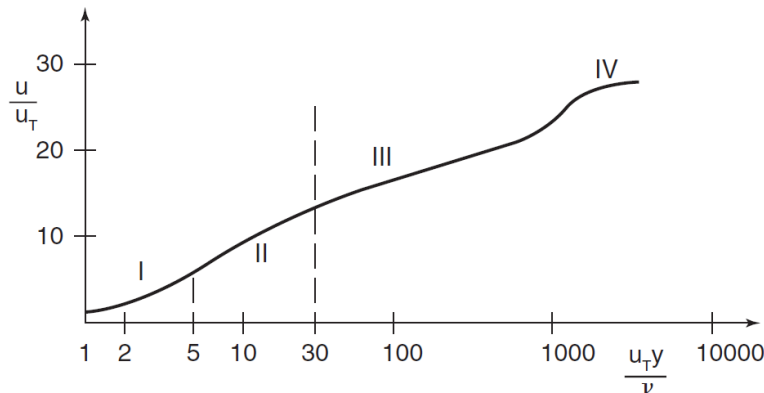


Figure 3.8 Regions of turbulent boundary layer. (Larsson & Raven, 2010)

Vertical axis represents x-directional velocity divided by friction velocity and horizontal axis represents nondimensional wall distance.

These four turbulent boundary layer regions are according to Larsson & Raven, (2010):

1. Viscous sublayer, where  $0 \leq y^+ \leq 5$ , and the velocity profile is linear.
2. Buffer layer, where  $5 < y^+ \leq 30$ , and the velocity profile changes from linear to logarithmic.
3. Logarithmic region, where  $30 < y^+ < 500 - 10\,000$ , and the velocity profile is logarithmic.
4. Wake region, which is between the logarithmic region and the edge of the boundary layer, where the velocity profile follows a logarithmic law to which the law of the wake is added.

In this two-dimensional representation of a boundary layer, three important effects are missing: streamline convergence in the lateral direction, and both longitudinal and lateral pressure gradients (Larsson & Raven, 2010). The turbulent boundary layer regions are of great importance in how boundary layer flow is treated in CFD simulations. This will be discussed further in Section 4.2.

### 3.4 Wake Field

The flow region leaving the aft of the ship hull is called the wake field. Since a ship's propeller operates inside the wake region, wake field characteristics are of great interest to ship designers.

Carlton (2019) names four main influences on wake field at the propeller:

1. The streamline flow around the body.
2. Growth of the boundary layer over the body.
3. The effect that the propulsor has on modifying the wake produced by the propelled body.
4. The influence of any wave-making components.

Total wake velocity arriving at the propeller consists of three components: nominal velocity, interaction velocity and propeller induced velocity. Nominal velocity is the flow arriving at the propeller plane in the absence of the propeller. When the propeller is added, it changes the flow field around the hull before it enters the propeller plane. These changes arise from the upstream influence on the flow by the propeller's presence (interaction velocity) and of the velocity induced at the propeller. The composition of the total flow velocity at the propeller plane is illustrated in Figure 3.9.

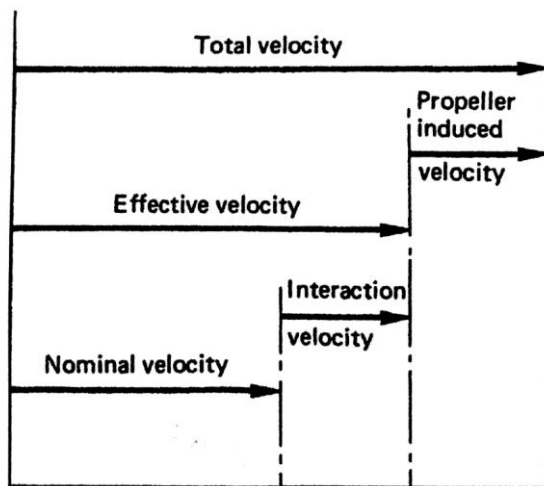


Figure 3.9 Total wake velocity composition. (Carlton, 2019)

It is commonly assumed that the wake field can be predicted from the nominal wake, meaning that interaction velocity and propeller induced velocity are not significantly modified by changes in nominal velocity. Nominal wake is commonly used for both propeller design and for optimizing a hull's stern form (ITTC, 2014a). Modeling the propeller's influence adds inaccuracies to the overall simulation. In addition, separating the effect of the propeller from total wake field is difficult. Because of these reasons, only the nominal wake field is considered in this thesis.

The ITTC recommends simulating wake at full scale when possible. However, there is a very limited quantity of validation data from full scale measurements, especially of nominal wake. (ITTC, 2011). Carlton (2019) mentions that the nominal wake field was measured in the Meteor trials of 1967. Measurement results from this study are presented in Figure 3.10.

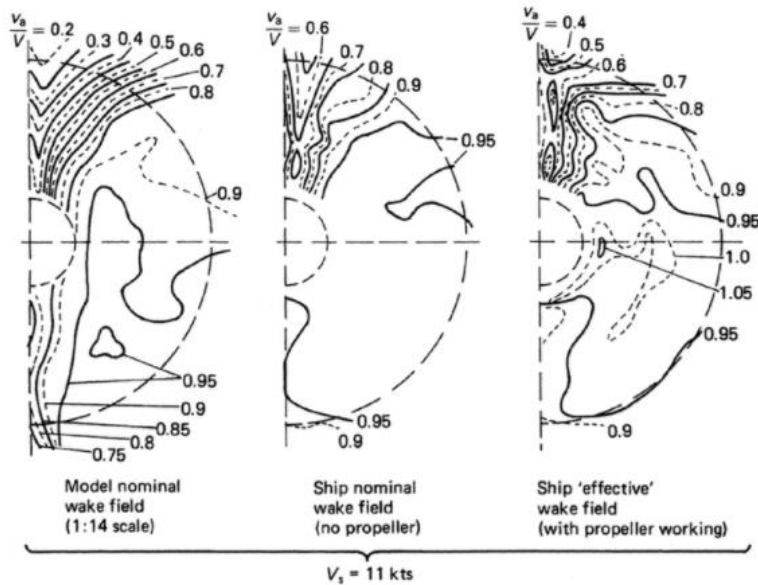


Figure 3.10 From the left. Difference between model scale nominal wake, full scale nominal wake and full scale effective wake from Meteor trials. (Carlton, 2019) Note that the axial velocity is denoted as  $v_a$  and the ship velocity as  $V$ , while  $v_x$  and  $V_s$  are used in this thesis, respectively.

As seen in Figure 3.10, nominal wake is noticeably less intensive at full scale compared to model scale, mainly due to difference in Reynolds number. The Reynolds number is typically of the order of  $10^6$  to  $10^7$  in model tests, while ships operate with Reynolds numbers around  $10^9$  (ITTC, 2011). Thus, both the wake's maximum values and the strength of the bilge vortex decrease in a full-scale wake when compared to model scale (ITTC, 2011). Furthermore, it is seen from the Figure 3.10 that velocity contours get distorted when the propeller's effect is included in the flow.

As presented by Carlton (2019), the effective wake field results from the interaction between the nominal wake field and the propeller:

$$\text{Effective velocity} = \text{nominal velocity} + \text{interaction velocity} \quad (7)$$

The nominal wake can again be broken into four parts: the potential, frictional, wave-induced wake components and the nonlinear interactions between frictional wake and wave-induced wake components (Carlton, 2019):

$$w_n = w_p + w_v + w_w + \Delta w, \quad (8)$$

where potential wake  $w_p$  represents the inviscid part of the flow, frictional wake  $w_v$  is caused by viscous effects in the flow and the wave-induced component  $w_w$  is the result of wave formation by the vessel. These do not add linearly; instead, the deviation from the linear composition is included with a nonlinear interaction term  $\Delta w$ .

Carlton (2019) mentions that the potential wake and wave induced components have only small effects on the total wake, especially with small Froude number vessels, based on research conducted by S.A. Harvald. In his experiments, Harvald found that the wave-induced

wake component has a very small amplitude (Harvald, 1950) and that friction wake is generally the largest component (Harvald, 1973). Due to these reasons, the friction wake component is in large role in nominal wake of the studied KVLCC2 hull.

There are three main definitions for wake: the Velocity ratio method, Taylor's wake fraction method and the nowadays less often used Froude wake fraction method (Carlton, 2019). These methods present the wake field with nondimensional components.

Nondimensional velocity ratios are defined in terms of individual flow velocity components at the propeller disk (axial, tangential and radial velocities,  $v_x$ ,  $v_t$  and  $v_r$  respectively), and the ship velocity,  $V_s$  (Carlton, 2019):

$$V_x = \frac{v_x}{V_s}, V_t = \frac{v_t}{V_s}, V_r = \frac{v_r}{V_s}, \quad (9)$$

where  $V_x$  denotes nondimensional axial velocity,  $V_r$  nondimensional radial velocity and  $V_t$  nondimensional tangential velocity, respectively.

The Taylor wake fraction for axial velocities is (Carlton, 2019):

$$w_T = \frac{V_s - v_x}{V_s} = 1 - \left(\frac{v_x}{V_s}\right) \quad (10)$$

The Froude wake fraction is (Carlton, 2019):

$$w_F = \frac{V_s - v_x}{v_x} = \left(\frac{V_s}{v_x}\right) - 1 \quad (11)$$

In this work, velocity ratios and Taylor's wake fraction are used.

The ITTC recommends presenting wake results in the following formats (ITTC, 2014a):

1. Contour plot of iso-lines of Taylor wake fraction  $w_T = 1 - V_x$ , including two circles to mark the radius of propeller hub and propeller tip.
2. Transverse components ( $V_r$ ,  $V_t$ ) plotted as velocity vectors in the propeller plane.
3. The three velocity components are provided in tables at a number (often 10) of radius or plotted as function of peripheral angles ( $\Phi$ ).
4. Nominal wake fraction  $w_n$  by integration of the axial velocity  $V_x$  over propeller disk.

In general, presentations showing iso-contours of a wake fraction's give a more nuanced view of the wake's characteristics than looking solely at the average wake fraction across the propeller plane. An example of such presentation is shown in Figure 3.11.

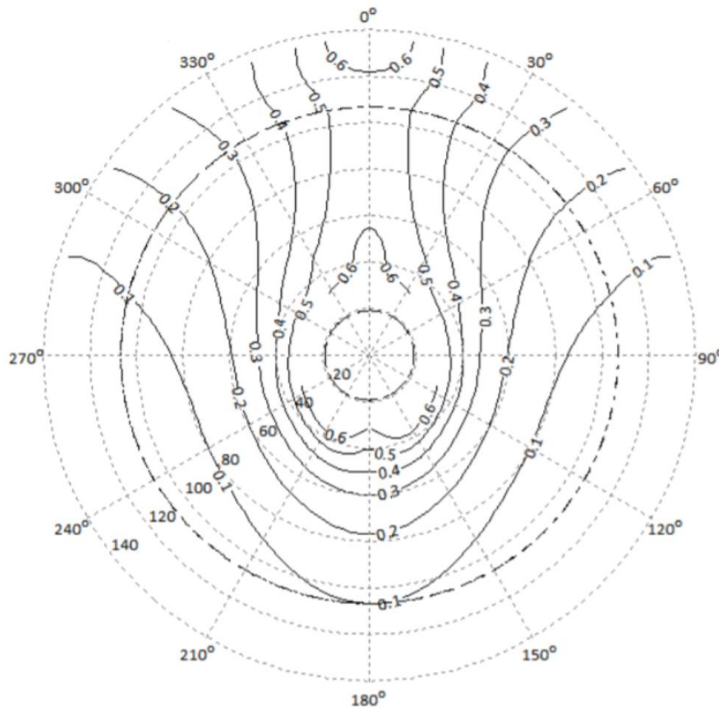


Figure 3.11 Wake fraction iso-contours. Dashed lines mark propeller hub diameter and propeller diameter. (ITTC, 2014a)

Peripheral angles are displayed at the outer radius of the circle in clockwise direction. Dashed lines mark the extents of propeller hub diameter and propeller diameter.

### 3.5 Methods for Wake Quality Assessment

In order to compare efficiency between different designs, the methods of wake quality assessment need to be defined. For example, propeller performance is affected by both the velocity and uniformity of the flow field: high wake fraction at the propeller increases thrust although it can increase friction resistance (Kim et al., 2001) and uniform flow results in less varying loads and smaller vibrations. Two key requirements for a good-quality wake field are therefore a high effective wake fraction and a small circumferential nonuniformity (Larsson & Raven, 2010).

According to Carlton (2019), three wake quality assessment methods have become widely used. These are the van Gunsteren and Pronk assessment method (van Gunsteren & Pronk, 1973), the Huse criteria (Huse, 1974) and the extensions to Huse criteria by Odabasi and Fitzsimmons (Odabasi and Fitzsimmons, 1978).

The methods from van Gunsteren and Pronk, and their extensions from Odabasi and Fitzsimmons, are related to cavitation and propeller-wake interaction. The Huse criteria, by contrast, deals with flow in a nominal wake field in the absence of a propeller. It will be the primary criteria used in this work.

Huse (1974) defines the relevant criteria for a large vessel wake in the absence of propeller as follows:

1. For large tankers and other ships with high block coefficients, the maximum measured wake should be less than 0.75 at 0.4-1.15R above the shaft center line:  
 $w_{max} < 0.75$
2. Maximum acceptable wake peak criteria at 0.7R:  $w_{max} < 1.7\bar{w}_{0.7}$
3. Width of the wake peak should be considered. Pressures on the hull are maximum in case of the width is slightly smaller than distance between propeller blades.

In these definitions,  $R$  is the propeller radius,  $w_{max}$  is the maximum wake at the center plane within 0.4-1.15R radius from the propeller hub and  $\bar{w}_{0.7}$  is the mean wake at a radius of 0.7R.

The wake peak is illustrated in Figure 3.12 according to Odabasi & Fitzsimmons (1978), as mentioned in Carlton (2019).

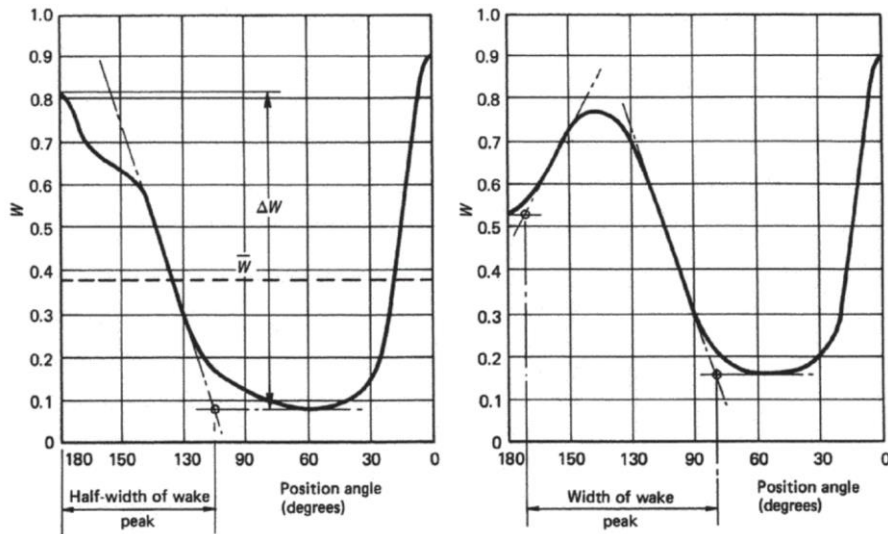


**Figure 3.12** Definitions of wake peak for single wake peak (left) and double wake peak (right). (Carlton, 2019)

On the left, the definition of half of a single wake peak is presented. On the right, width of a double wake peak is presented. The height of the peak is denoted as  $\Delta w$ .

## 4 Applied Methods

This chapter describes the methods and software applied in the simulation. Recommendations based on previous research are reviewed.

Rhinoceros 3D version 5 was used for improving quality of a hull surface file which was in IGES-format. For transforming IGES-file to STL-format, NAPA Designer 2020.1 was used. NAPA 2020.1-1 was used to generate a body plan view of the hull. The computational grid was constructed, and simulations were conducted using the StarCCM+ software version 15.04.008. Paraview, which is a free open source software, was used to visualize the results. The Paraview versions used were 5.4.1 and 5.8.

### 4.1 Grid Generation

The ITTC Practical Guidelines for Ship CFD Applications (ITTC, 2014b) and for RANS Calculation of Nominal Wakes (ITTC, 2014a) were used as guidelines for grid generation. These guidelines include recommendations on the size of computational domain, grid generation and grid aspect ratios. Some of these instructions are included here and they are as follows:

- It is recommended to use hexahedral grids for wake estimation.
- Grid should be refined between aft shoulder of the hull and propeller plane
- Wall functions: first grid point should be clearly inside logarithmic boundary layer region. Recommended values are  $30 < y^+ < 100$ . Within boundary layer, at least 15 points should be included.
- Wall-resolved turbulence model: recommended distance is  $y^+ < 1$ . Within boundary layer, at least 20 points should be included.
- Expansion ratio is recommended to be 1.2 or less. The largest acceptable value is 1.5 for near-wall turbulence solving.
- Bilge keels, stabilizer fins, ducts and pre-swirl stators should be included in hull geometry. For open-shaft vessels, shafts and brackets should be included.

Because the KVLCC2 benchmark vessel has been widely simulated with a bare hull, no attachments were included in this study's geometry.

Gothenburg 2010 Workshop results (Larsson et al., 2014) showed that around 3 million grid points on a double body simulation showed good agreement on resistance with towing tank test results. Mean comparison error was approximately 4% for grids larger than 3 million cells, but approximately 8% for grids smaller than 3 million cells. Larsson et al. (2014) mentions that, based on their experiments, a mesh with around 3-4 million cells is dense enough for modeling error to dominate discretization error.

Figure 4.1 visualizes the results from several different hull forms in Gothenburg 2010 Workshop. It is to be noted that, unlike the two other hull forms, the KVLCC2 hull is from the low Froude number range.

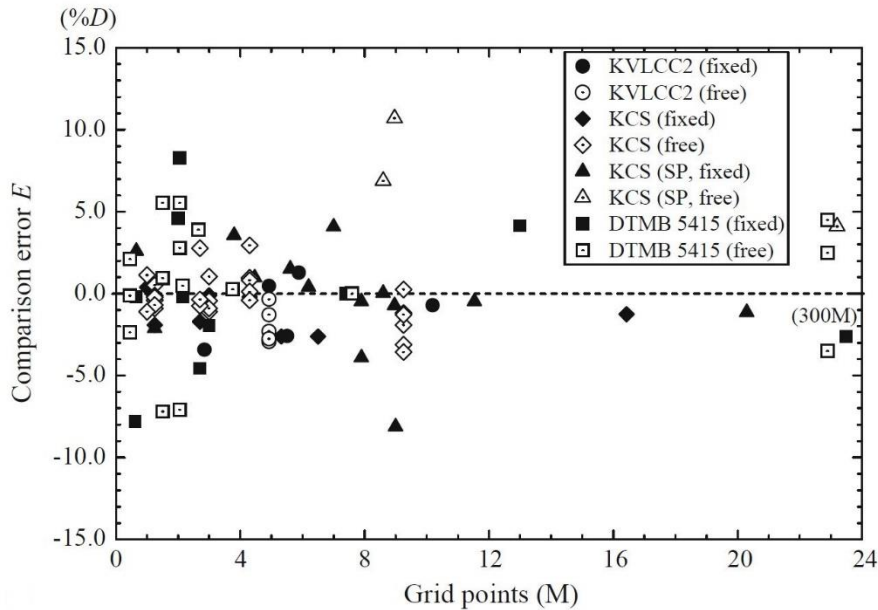


Figure 4.1 Comparison error with respect to the amount of grid points used. (Larsson et al., 2014)

Resistance predictions are not significantly more accurate when mesh size is increased to over 4 million cells, although there is no systematic mesh refinement present. However, these results for resistance do not necessarily mean that wake field predictions do not benefit from an increased number of grid points. Larsson & Raven (2010) mention that the wake field at the propeller plane is one of the most resolution-dependent aspects in ship resistance assessment.

## 4.2 Turbulence Modeling

Due to the highly turbulent characteristics of the flow around ships, RANS equations alone do not describe the flow accurately. The effects of strong turbulence can be modelled more accurately either directly, using models that capture turbulent eddies, or indirectly, using turbulence models with average turbulence characteristics. The first approach includes the Large Eddy Simulations (LES) technique, in which large eddies are simulated and small ones are filtered out, and the related Detached Eddy Simulations (DES) technique. Research with LES and DES has been conducted on ship cases (Larsson et al., 2014), although these methods remain computationally heavy. For instance, one billion grid points and 1 536 computing cores were used in a model scale large eddy simulation of KVLCC2 by Nishikawa et al. (2012).

Another technique is the Direct Numerical Simulations (DNS). These are currently too computationally heavy to be used for solving the flow around a ship: Nishikawa et al. (2012) estimates that cost of a DNS is typically hundred to thousand times larger than a LES. DNS may become a usable, accurate approach in the more distant future.

Due to these reasons, turbulence models have remained as the favored solution for ship design (Carlton, 2019), accompanied by towing tank tests. The shear stresses caused by highly turbulent flow are modelled as so-called effective viscosity  $\mu_{eff}$ , consisting of dynamic viscosity  $\mu$  and turbulent viscosity  $\mu_t$  (Larsson & Raven, 2010):

$$\mu_{eff} = \mu + \mu_t \quad (12)$$

There are numerous models for including turbulent viscosity in the flow. All turbulence models used for ship flows are semi-empirical (Bertram, 2012), and their accuracy and usefulness depend on the intended use. The ones used commonly in ship CFD applications include  $k-\epsilon$ , Reynolds stress model and versions of  $k-\omega$ . ITTC (2011) mentions that SST  $k-\omega$  and Reynolds stress models in particular provide good correlation in wake field prediction, although according to ITTC (2014a), advanced turbulence models provide more accurate results in wake field prediction than simpler (isotropic) turbulence models, especially for ships with full hull forms like the tanker vessel studied in this thesis. ITTC (2014a) recommends using RSM (Reynolds Stress Model), EARSM (Explicit Algebraic RSM) or rotation corrected SST  $k-\omega$  models if possible.

There are two ways for solving boundary layer flow with turbulence models. In the first, the flow is solved for near the wall within a laminar sub-layer using a near-wall turbulence model. The advantage of this is increased accuracy, at the cost of higher cell aspect ratios near the wall (the first point is generally recommended to be within  $y^+ < 1$ ) and increased computing times. In the second approach, wall functions which utilize a mathematical model of the inner boundary layer are used, and the calculated points are set to begin in the logarithmic region,  $y^+ > 30$ . With wall functions, the required grid is coarser, resulting in computations which are generally faster and more stable. However, wall functions are based on two-dimensional boundary layer flow which, as mentioned in Section 3.3, differs slightly from the physics of three-dimensional flow. Larsson & Raven (2010) mention that wall functions cause deviations especially if flow is strongly three-dimensional, the boundary layer is thick or if there is separation of flow.

At grid sizes larger than 3 million cells, comparison error for the SST  $k-\omega$  turbulence model remained less than 5 % in tested cases (Larsson et al., 2014). Figure 4.2 presents turbulence models tested at the Gothenburg 2010 Workshop and their respective comparison errors.

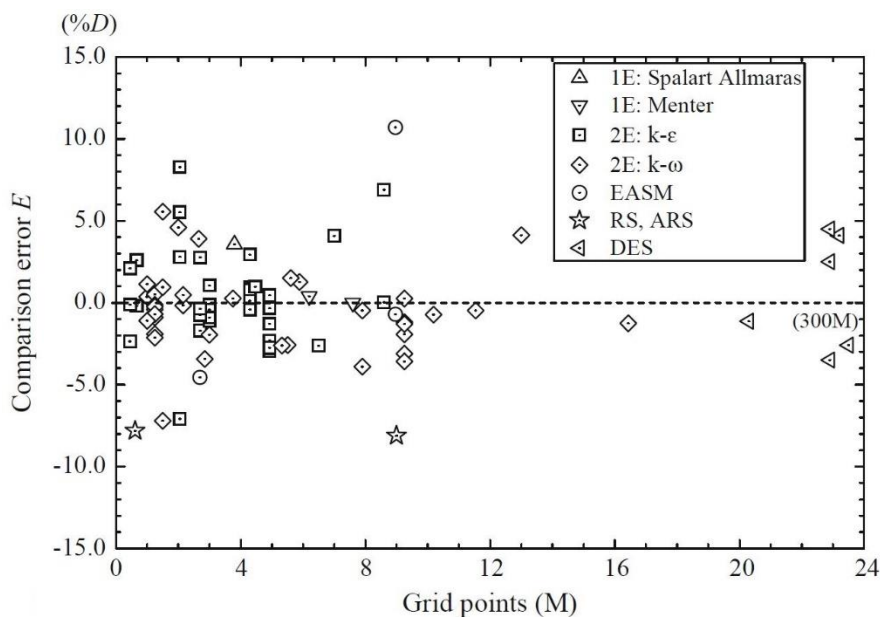


Figure 4.2 Comparison error with different turbulence models. (Larsson et al., 2014)

The results for comparison errors of  $k-\omega$  turbulence model were within 6% comparison error, although the data is limited, and tested hull forms varied.

### **4.3 Discretization Methods**

The accuracy of the solution depends on the accuracy of numerical methods used, and large inaccuracies induced by the numerical methods are to be avoided. However, the selection of a numerical scheme is a balance between accuracy, stability and computation time. ITTC (2014b) mentions that since the first-order upwind scheme induces high numerical diffusion when solving a convection-diffusion equation, a second-order accuracy is the minimum for solving flow around a ship. Solvers with higher orders of accuracy are available, although they may be less stable or more computationally complex. First-order accuracy in time can be used in steady state solutions only (ITTC, 2014b).

At the Gothenburg 2010 ship hydrodynamics workshop each group utilized second-order discretization schemes on the KVLCC2 test case (Larsson et al., 2014). Five years after this, at the Tokyo 2015 workshop, most groups continued to use second-order discretization schemes (Hino et al., 2021). Time accuracy was of first or second order. Based on these findings, a second-order upwind scheme was selected for solving the convection terms.

## 5 Simulation Set-Up

This chapter presents the research case vessel, the KVLCC2 (Korean Very Large Crude Carrier 2). Grid generation for the simulation is discussed, and the mathematical models used in the simulation are presented. The simulation files are presented in appendices.

The hull surface was obtained from SIMMAN (2008) in IGES-format. In NAPA Designer, the hull surface was intersected with help lines in order to increase the quality of the transformation to STL-format. The help lines were added primarily in the bow and aft sections.

The mesh was initially meant to be generated using the OpenFOAM mesher snappyHexMesh. However, there were difficulties with this approach, especially in laying a sufficiently thin prismatic layer on the hull surface. Unsuccessful attempts led to using of the Star-CCM+ mesher instead. Problems with the utilization of snappyHexMesh have been reported in other master theses as well; for example, Esquivel de Pablo (2013) and Asén (2014) reported unsuccessful attempts in generating high quality mesh using snappyHexMesh and decided to use the Numeca International tool HEXPRESS instead.

### 5.1 Case study

KVLCC vessels KVLCC, KVLCC2 and KVLCC2M are CFD test case models designed by KRISO (Korean Research Institute of Ships and Ocean Engineering) in the late 1990s. Their size and dimensions represent the commercial very large crude carriers of the era (Kim et al., 2001), and they have been since widely used in both CFD workshops and research. The KVLCC2 variant was chosen to be the hull studied for this thesis because it had been so widely studied in numerous CFD workshops.

Simulation results of model scale towing tank tests and CFD tests in model scale are publicly available. None of the KVLCC hull versions have been built in full scale so actual full-scale measurement data was not available. The wetted hull surface area was approximately 1.3% larger than one mentioned in literature for model scale hull. Table 5.1 presents the main particulars and propeller information.

**Table 5.1 Main particulars of KVLCC2 in full and model scale. Combined from Larsson et al. (2014), Kim et al. (2001), SIMMAN 2008 (2008) and from the used hull model.**

Quantity	Symbol	Unit	Full scale	Simulated model (1:58)
Length between perpendiculars	L <sub>pp</sub>	m	320	5.5172
Breadth	B	m	58	1
Draft	T	m	20.8	0.3586
Speed	v	m/s	7.9739	1.047
Froude number	Fn		0.142	0.142
Reynolds number	Re		$2.1 \cdot 10^9$	$4.6 \cdot 10^6$
Displacement	$\Delta$	m <sup>3</sup>	312 622	1.6029
Wetted surface area (without rudder)	S	m <sup>2</sup>	27194	8.2319
Block coefficient	C <sub>B</sub>		0.8098	0.8098
Vertical center of gravity	KG	m	18.6	0.3207
Propeller location		m	5.6	0.09655
Propeller diameter		m	9.86	0.17
Propeller hub diameter		m	1.53	0.0264

The chosen boundary conditions and fluid properties are presented in Tables 5.2 and 5.3. Constant velocities and turbulences were applied at inlet and at sides, except symmetry condition was applied at the top and at the symmetry plane. Density of the water was set constant.

**Table 5.2 Boundary conditions**

Boundary	Condition
Inlet	Constant velocity, constant turbulence
Outlet	Constant static pressure
Top	Symmetry
Bottom	Constant velocity, constant turbulence
Portside	Constant velocity, constant turbulence
Symmetry plane	Symmetry
Hull	No-slip

**Table 5.3 Fluid properties**

Quantity	Symbol	Unit	Value
Dynamic viscosity	$\mu$	Pa·s	8.8871E-4
Water density	$\rho$	kg/m <sup>3</sup>	997.561 (constant)

The studied hull form features a high bulbous bow and a box shaped mid ship section. Figures 5.1-5.3 present the body plan, aft view of the hull with location of the propeller and side view of the hull with location of the propeller.

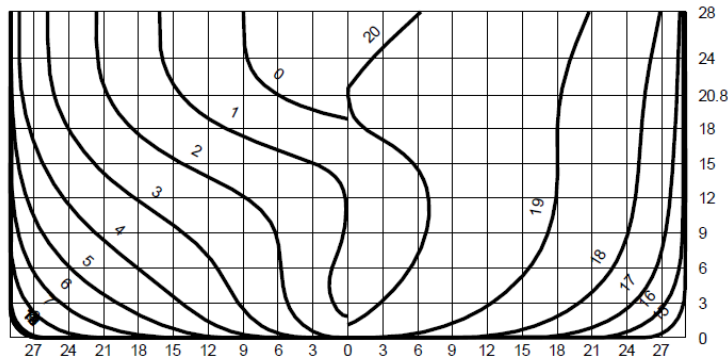


**Figure 5.1** Body plan.

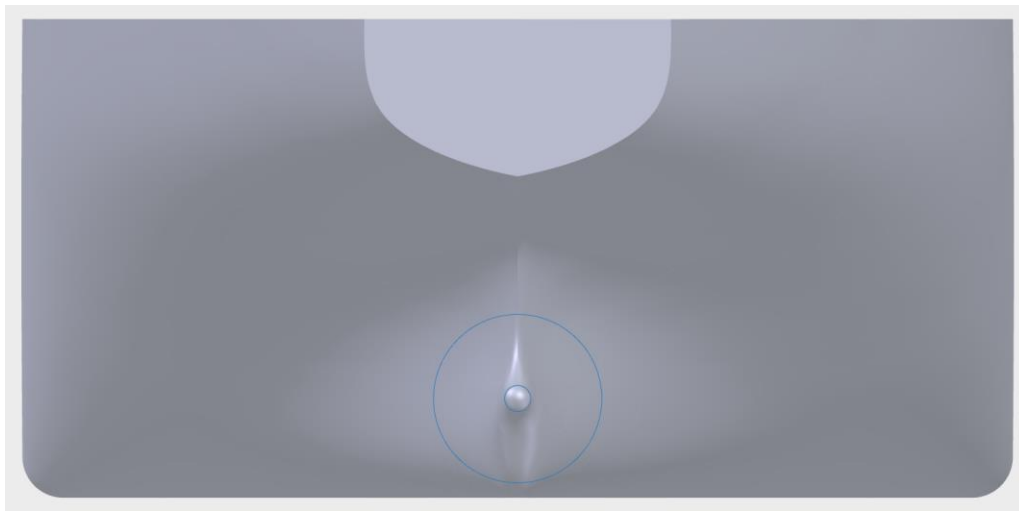


**Figure 5.2** Propeller and propeller hub location, aft view.

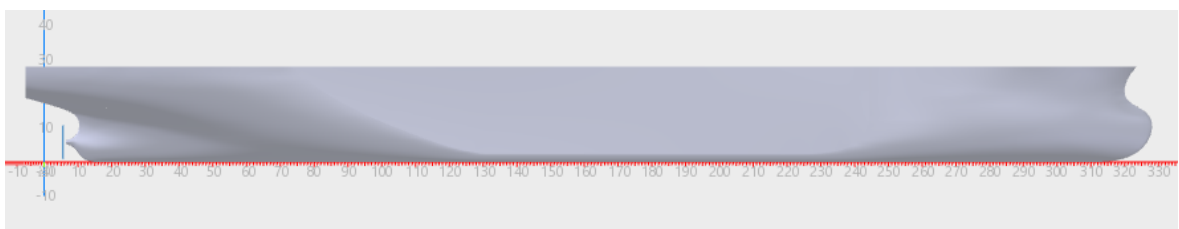


**Figure 5.3** Propeller location, side view.

## 5.2 Computational grids

Computational grids were constructed based mainly on ITTC recommended procedures (ITTC 2014a, ITTC 2014b) and results from the Gothenburg Workshop 2010 (Larsson et

al., 2014). Some deviations from the recommended procedures were done, and they are explained below. The two main parameters considered when generating the mesh were boundary layer thickness and the thickness of the first prismatic layer cell.

Boundary layer thickness  $\delta$  was estimated at the midship section. The common way of estimating this is to use the power law according to Schlichting (1987), mentioned by Larsson & Raven (2010). The power law is presented as:

$$\delta = \frac{0.37x}{\sqrt[5]{Re_L}}, \quad (13)$$

where  $x$  is distance along the hull from the bow and  $Re_L$  is the local Reynolds number at the location. This gives an approximate midship estimate of model-scale boundary layer thickness of 0.05m. However, when generating the mesh, better mesh quality was achieved when using a smaller thickness. Because of this, inside the boundary layer there are approximately 25 cells at the midship section, out of which 20 are prismatic layer cells. Although this is within the previously mentioned ITTC recommendations, Larsson & Raven (2010) recommend using at least 30 cells inside the boundary layer.

The ITTC 1957 friction line (ITTC, 1957) was used to estimate the frictional resistance coefficient  $C_f$ :

$$C_f = \frac{0.075}{[\log_{10}(Re_L) - 2]^2}, \quad (14)$$

where  $Re_L$  is the local Reynolds number. This was used for estimating the required height of the cell so that the nondimensional wall distance  $y^+$  is in the recommended range for a wall-resolved turbulence model, according to Equation 15 (ITTC, 2014b):

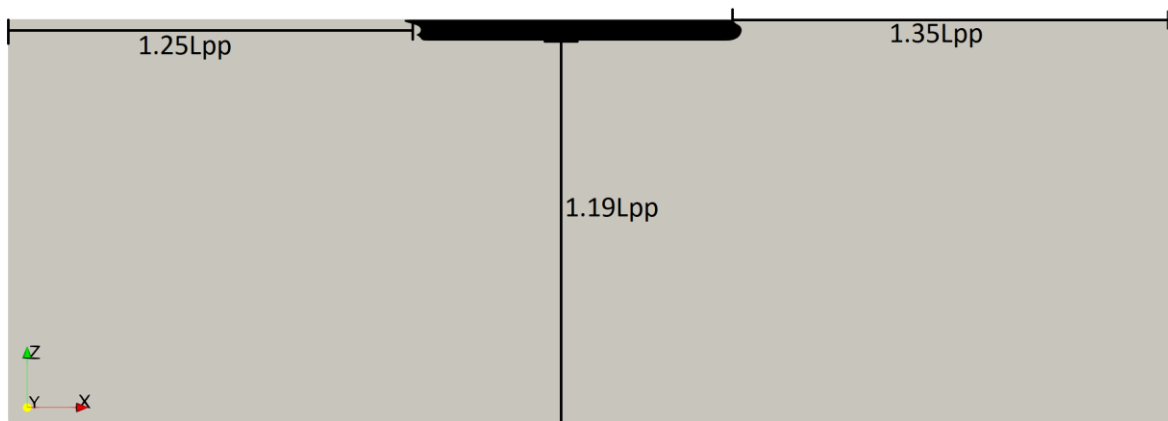
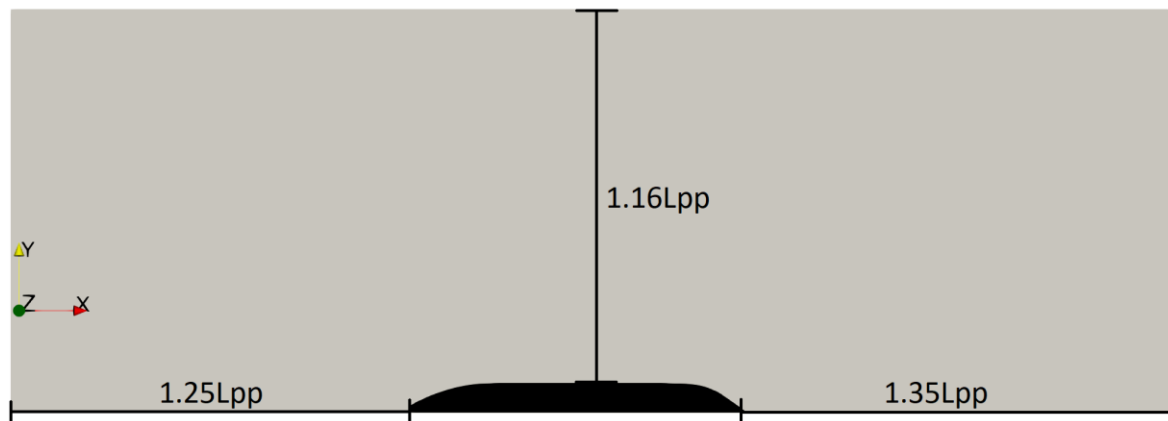
$$y = \frac{y^+L}{Re_L \sqrt{\frac{C_f}{2}}}, \quad (15)$$

where  $L$  is the distance along the hull.

An expansion ratio of 1.26 in the prismatic layer was selected since the value 1.2 recommended by ITTC (2014a) resulted in decreased grid quality. Larsson et al. (2014) mentions that accuracy had no clear dependency on the grid refinement ratio used during the Gothenburg 2010 workshop, where a refinement ratio of 1.2 was the most common choice. The mesh was sized according to ITTC recommendations (ITTC, 2014a): distances of at least 1.0 length between perpendiculars ( $L_{pp}$ ) should be left between the hull and inlet, outlet, side and bottom. Table 5.4 presents the mesh parameters used and Figures 5.4 and 5.5 visualize dimensions of the computational grid.

**Table 5.4 Mesh parameters**

Mesh size	7 365 047	cells
X	19.83 (3.59 $L_{pp}$ )	meters
Y	6.90 (1.25 $L_{pp}$ )	meters
Z	6.90 (1.25 $L_{pp}$ )	meters
Prismatic layer thickness	$1.38 \cdot 10^{-2}$	meters
Prismatic layer growth ratio	1.26	
Number of prism layers	20	
Inner layer thickness	$3.56 \cdot 10^{-5}$	meters
Cell length at prismatic layer	$5.52 \cdot 10^{-3}$	meters
Cell side dimensions at propeller plane	$2.76 \cdot 10^{-3}$	meters

**Figure 5.4 Computational grid dimensions (view from side).****Figure 5.5 Computational grid dimensions (view from up).**

Cells were gradually refined towards the hull by halving the length of each edge, dividing each cell into 8 new cells. The dimensions near the hull, but still outside the prismatic layer, were  $5.52 \cdot 10^{-3}$  m in length, width and height. More refined areas were included in the aft hull section. Out of these, a larger refinement area (starting from the end of the bilge keel, Figure 5.7) was constructed using anisotropic cells to reduce the number of total cells. The region around the aft perpendicular (Figure 5.8) was constructed of isotropic cells.

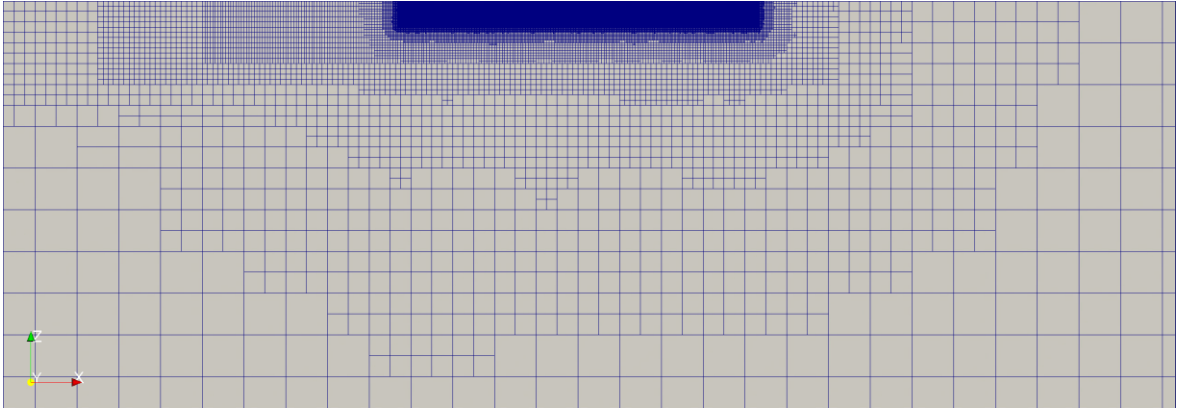


**Figure 5.6 Full mesh.**

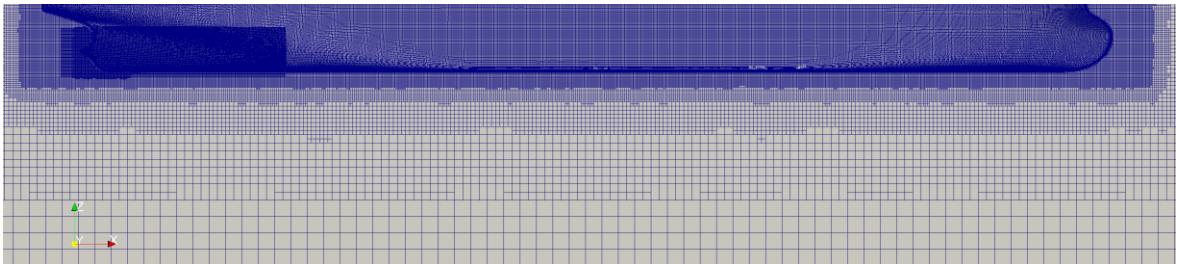


**Figure 5.7 Mesh around hull.**

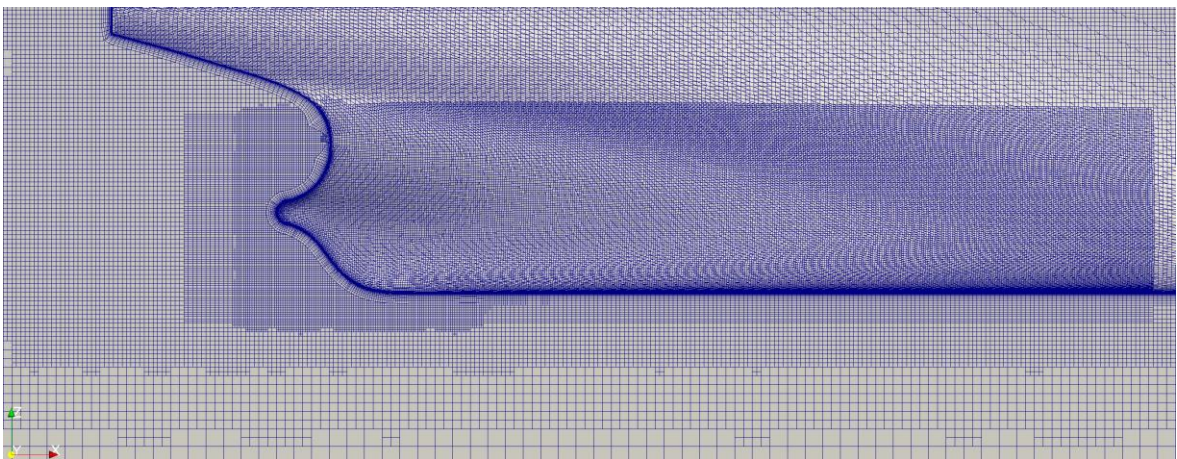


**Figure 5.8 Mesh on the aft hull.**

In the prismatic layer of the aft hull mesh (Figure 5.9), irregularities in the prismatic layer mesh appears in the upper left corner. The mesh generation parameters were adjusted in order to minimize the impact on grid quality in this region. In this region prismatic layer thickness collapsed from 20 to 17 cells, and cell shapes were distorted. Local flow in this region was monitored and it was concluded that there was no significant impact on the results.

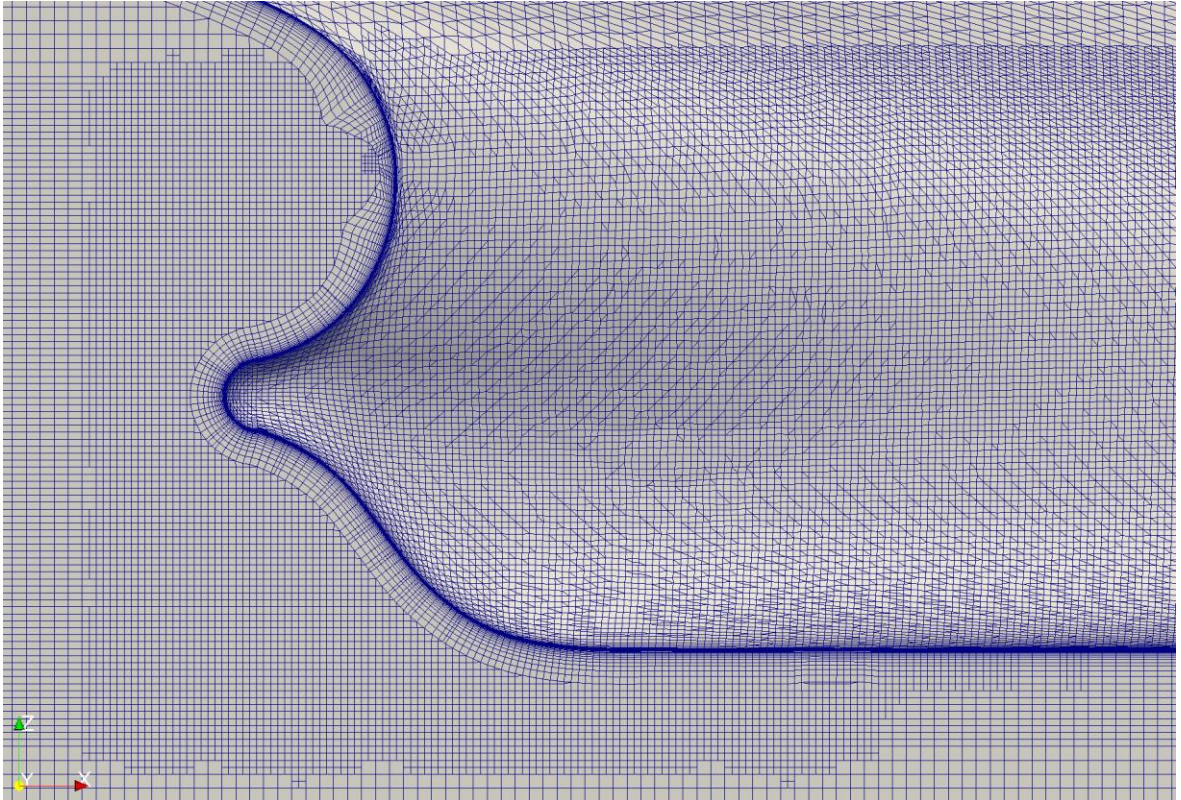


**Figure 5.9 Prismatic layer.**

For the grid sensitivity study, a refinement factor of 1.3 was used and mesh densification regions remained unchanged. The cell growth ratio was increased in order to keep growth of  $y^+$  to a minimum, while the number of layers in the prismatic layer decreased on each refinement. The aim was to keep the cell growth ratio constant. For this, the cell growth ratio of each round was estimated using the following relation:

$$q_f^r = q_c, \quad (16)$$

where  $q_f$  denotes the cell growth ratio in the finer mesh,  $r$  is the refinement factor and  $q_c$  is the cell growth ratio in the coarser mesh. It should be noted that the coarsest grid in particular is outside of the ITTC (2014a) recommended range: the cell growth ratio exceeded the largest acceptable value of 1.5, and  $y^+$  reached values of approximately 2 in the midship section. Table 5.5 shows the mesh parameters used.

**Table 5.5 Mesh parameters for grid sensitivity study**

Referred as	Refinement factor used	Grid size	Prismatic layer cells	Cell growth ratio	Minimum thickness (m)
"15.2M"	0.77	15 192 824	26	1.19	$2.9 \cdot 10^{-5}$
"7.4M"	1	7 365 047	20	1.26	$3.6 \cdot 10^{-5}$
"3.6M"	1.3	3 580 448	15	1.36	$5.0 \cdot 10^{-5}$
"1.8M"	1.69	1 803 943	12	1.47	$6.4 \cdot 10^{-5}$
"0.9M"	2.22	896 578	9	1.67	$9.2 \cdot 10^{-5}$

### **5.3 Workflow**

After a satisfactory grid was generated, the simulation parameters were set. In general, a simpler (and more stable) turbulence model was used to stabilize the solution. This solution was then used as a starting point for simulations using a more advanced turbulence model. However, the finest meshes with curvature corrected cubic turbulence model did not converge with these steps. Instead, the following methods were used.

For the 7.4M cell mesh, the starting point was mapped from the converged solution of the 3.6M cell mesh. For the 15.2M cell mesh, a stable solution was not achieved via the sole use of this method. Instead, the simulation was run with an implicit unsteady solver until a stable solution was achieved. This result was then used as a starting point for the steady solver, resulting in a converged solution.

Simulations were considered converged according to ITTC (2014a) recommendations: “the decrease of scaled residuals by at least three orders of magnitude from their initial values”.

## 6 Results and Discussion

This chapter presents the results from the case studies. The chapter is divided in three sections. First, results from grid sensitivity study are presented. The second section presents results from turbulence model comparison study. In the third section, the results and findings from the studies are discussed. The residual plots from the simulations are provided in appendices.

The results are presented as axial velocity iso-contours, wake fraction intensities and transverse velocity components for each case, and then plotted against peripheral angles at four radiuses. Then, simulation results are compared to towing tank tests, wind tunnel tests and to results from recent CFD studies.

### 6.1 Grid sensitivity study

The grid sensitivity study exclusively made use of the cubic SST  $k-\omega$  turbulence model with curvature correction.

The left-hand side of Figures 6.1-6.5 shows iso-contours of the axial velocity and the right-hand side shows wake fraction across the propeller plane. These are presented for the three tested turbulence models. The colors on the right side of the figures show the intensity of the wake fraction, while the overlaid vectors represent the flow's transverse velocity components. The length of each vector represents the transverse flow's strength. Note that the transverse velocity components are not distributed evenly between the figures but as a function of grid spacing.

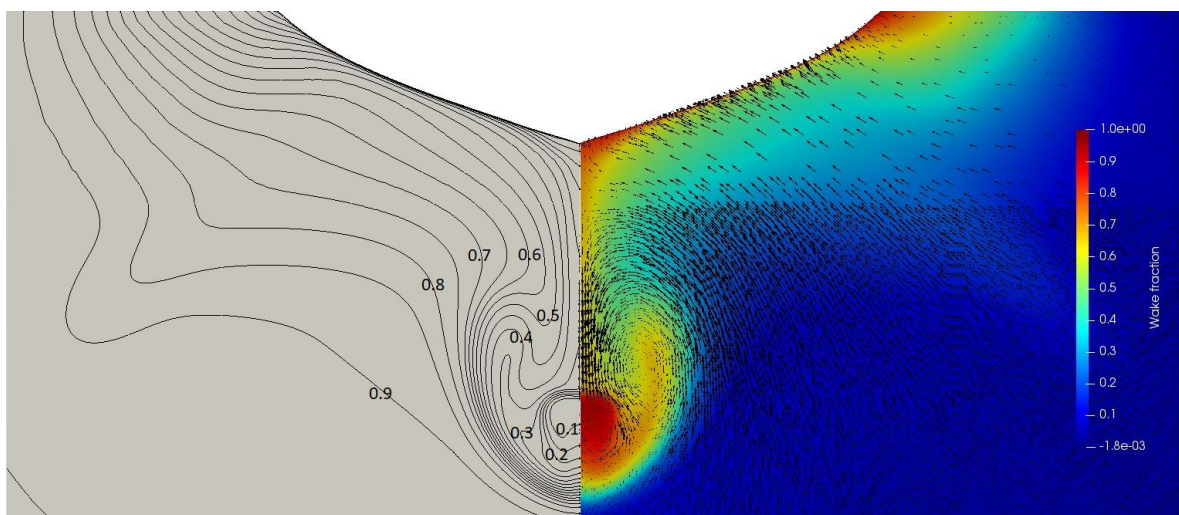


**Figure 6.1** Axial velocity ratio iso-contours (left), wake fraction and transverse velocity vectors (right). 15.2M cells

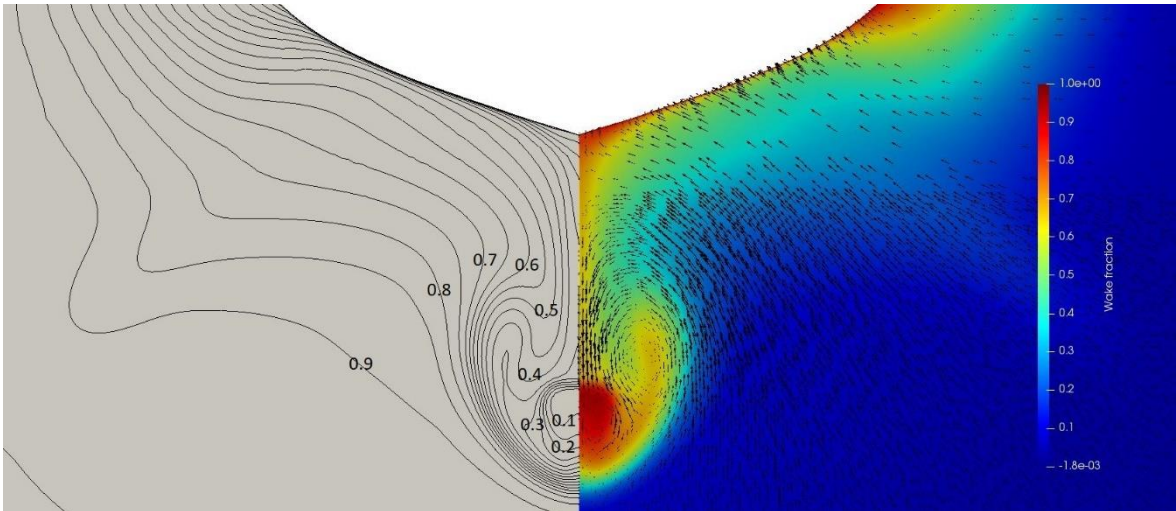


**Figure 6.2 Axial velocity ratio iso-contours (left), wake fraction and transverse velocity vectors (right). 7.4M cells**

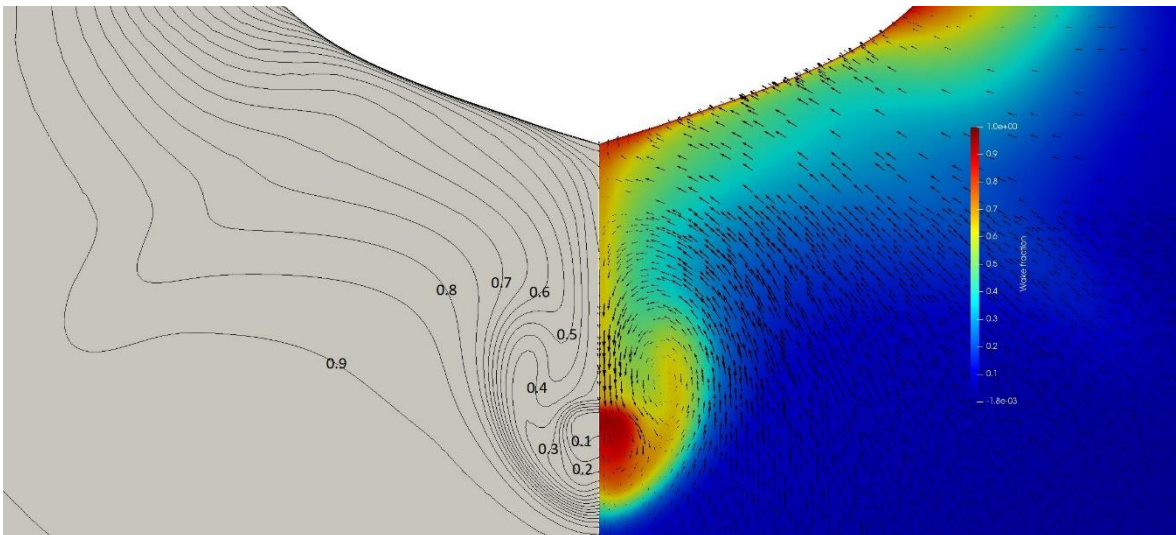


**Figure 6.3 Axial velocity ratio iso-contours (left), wake fraction and transverse velocity vectors (right). 3.6M cells**

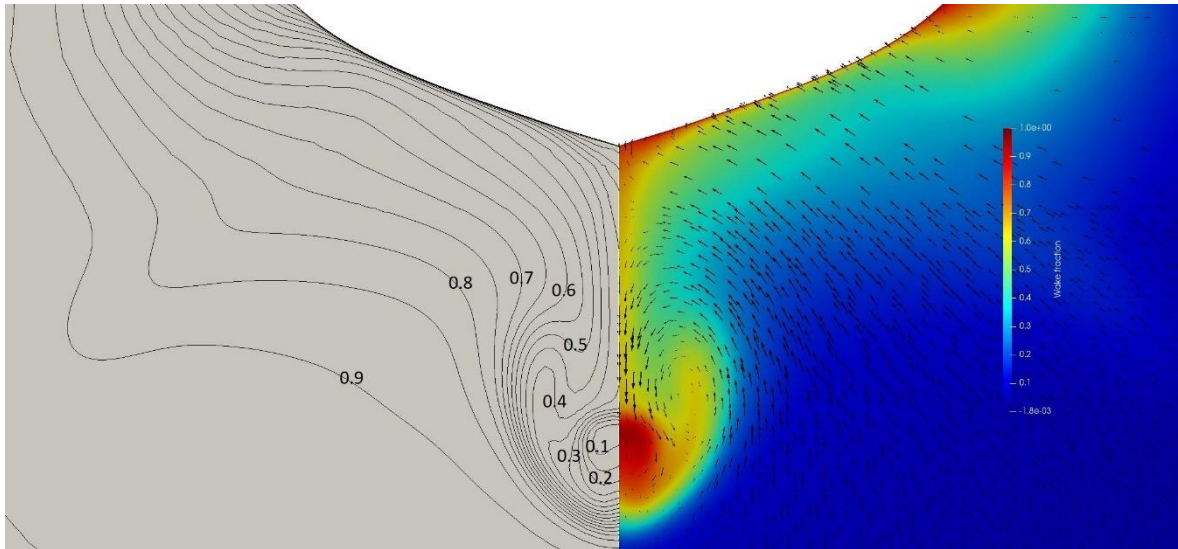


**Figure 6.4** Axial velocity ratio iso-contours (left), wake fraction and transverse velocity vectors (right). 1.8M cells

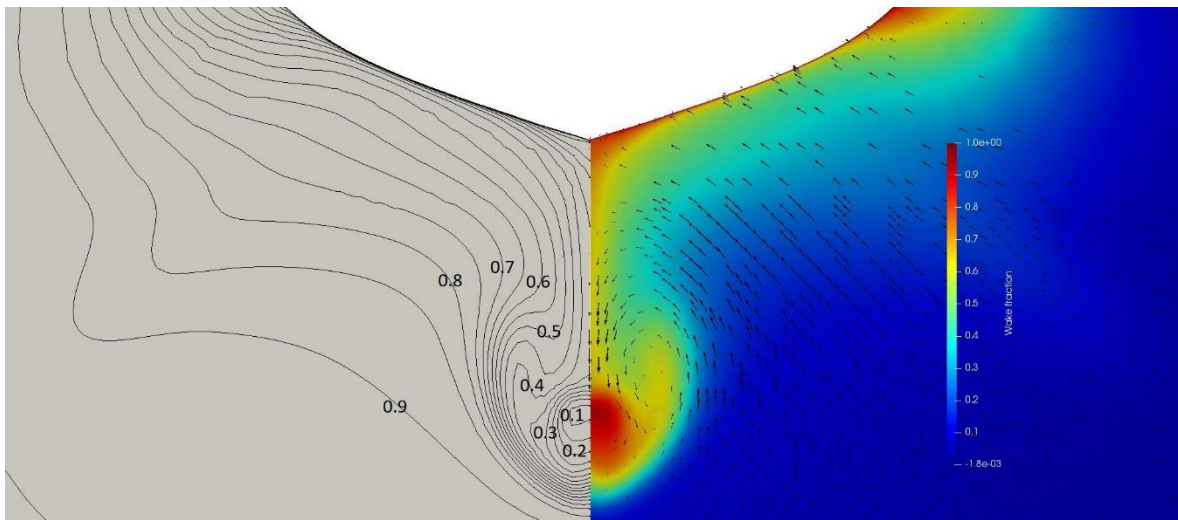


**Figure 6.5** Axial velocity ratio iso-contours (left), wake fraction and transverse velocity vectors (right). 0.9M cells

All the grids predicted the shape of bilge vortex rather accurately, although its intensity varies. The vortex strength decreases towards less refined grids. It is seen that even between 3.6 and 7.4 million cell grids there is a noticeable difference in the vortex's predicted strength.

The Figures 6.6-6.9 present axial wake fraction against peripheral angles at four radiuses from the propeller center. The peripheral angles ( $\Phi$ ) are defined as the clockwise angle, from the uppermost part of the propeller plane. The area in near proximity of the propeller hub is not considered due to reference data and because the propeller hub has large impact on the flow in the area since it was not included in the simulations.

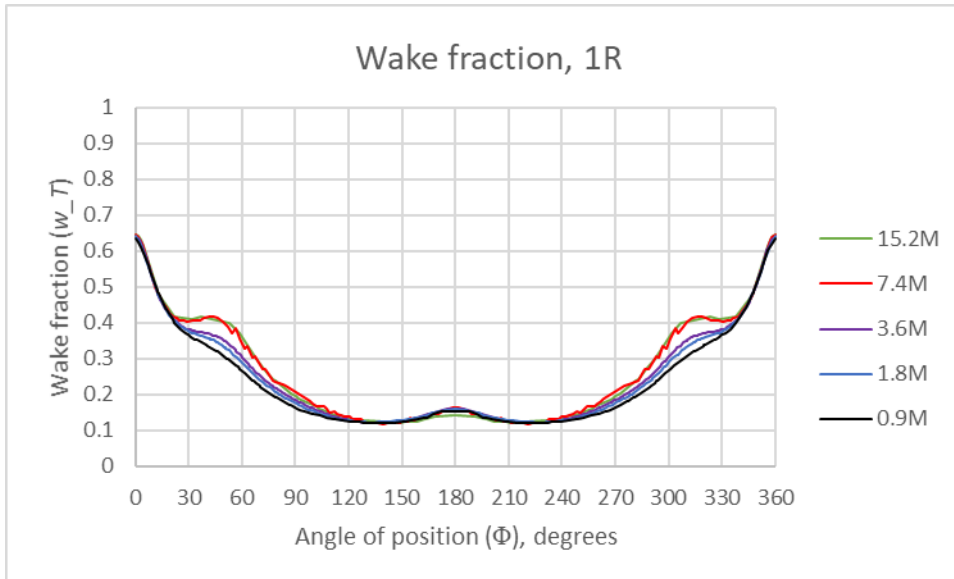


Figure 6.6 Axial wake fraction against peripheral angles, 1R.

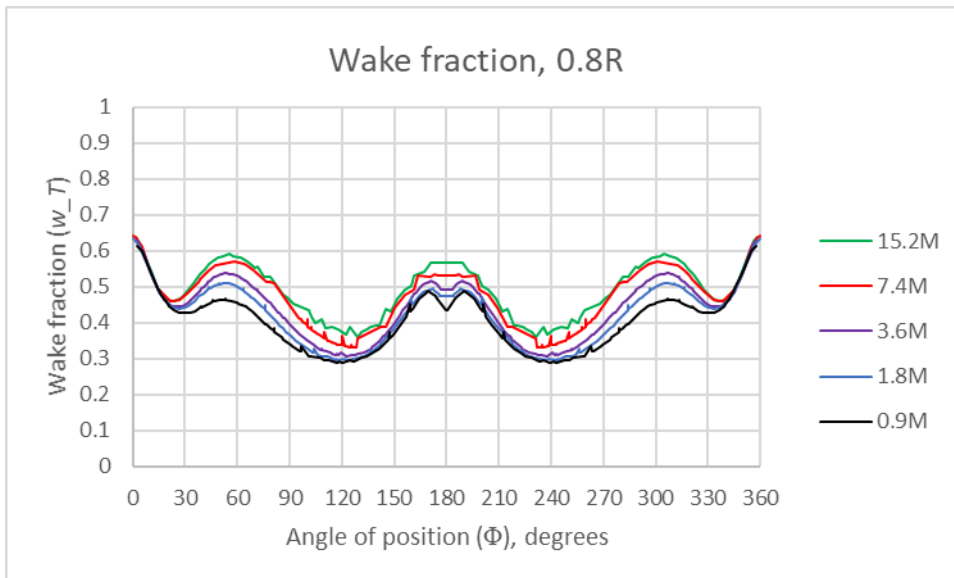
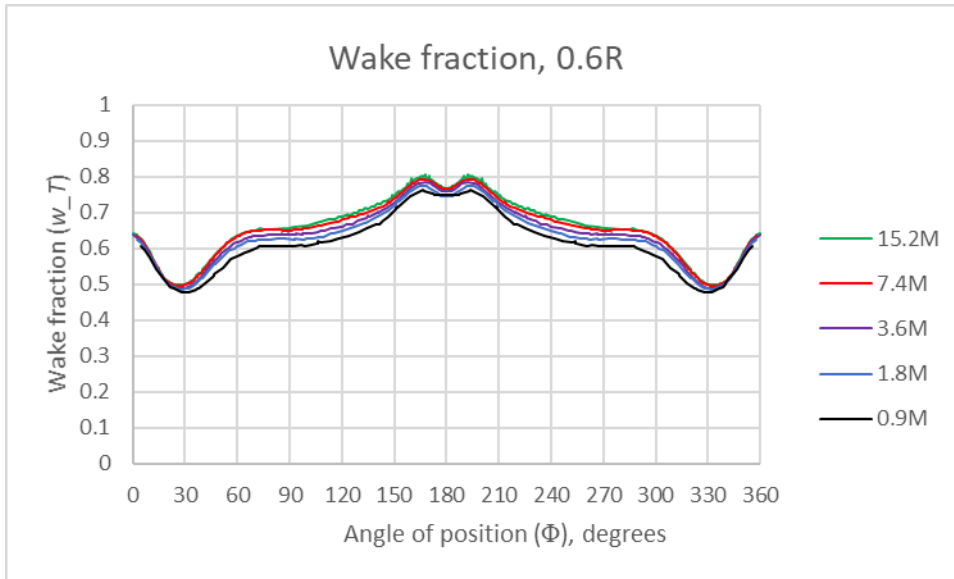
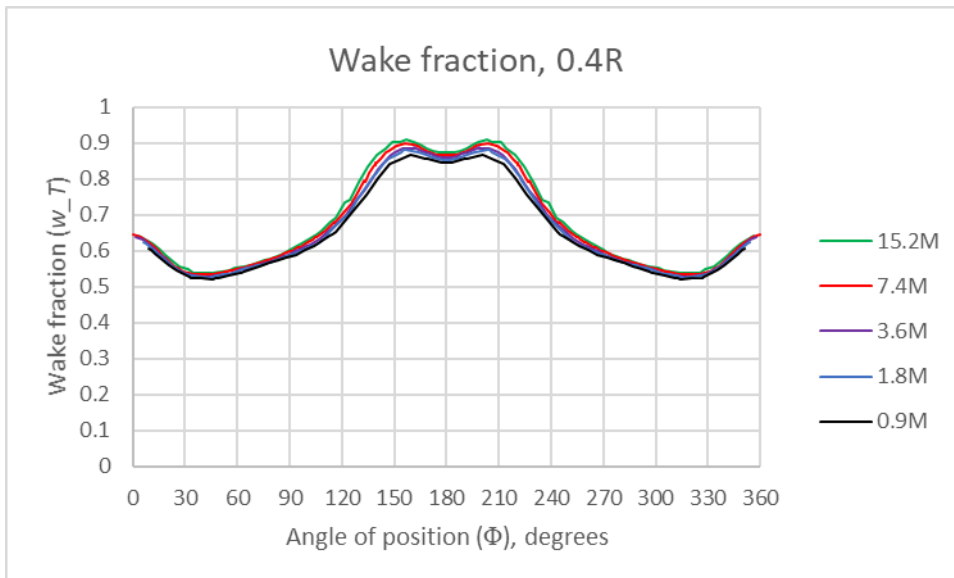


Figure 6.7 Axial wake fraction against peripheral angles, 0.8R.



**Figure 6.8 Axial wake fraction against peripheral angles, 0.6R.**



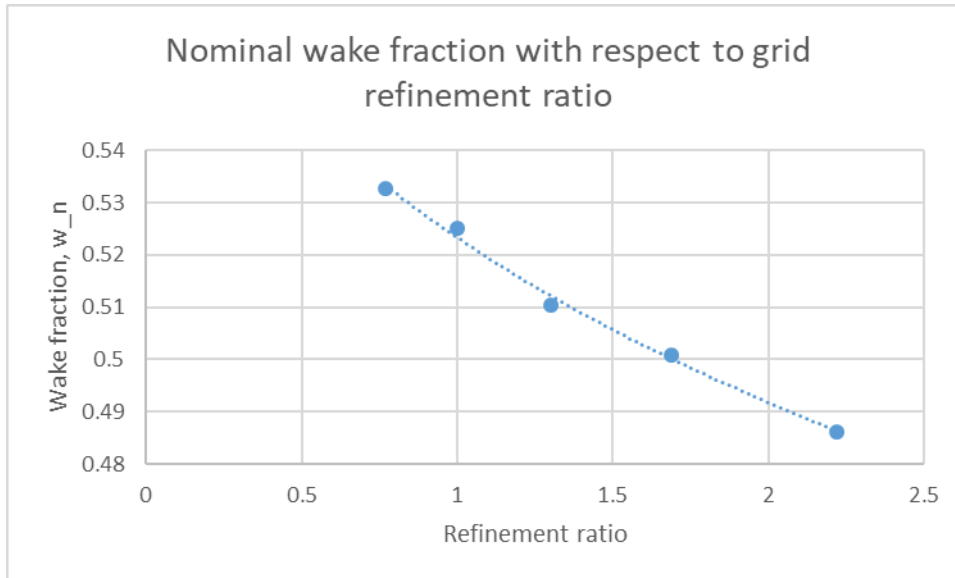
**Figure 6.9 Axial wake fraction against peripheral angles, 0.4R.**

Based on the presented figures, the wake fractions at each radius mostly seem to converge as the mesh is refined. However, this is less true at around  $0.8R$  and  $1R$  from the propeller hub, where results diverge with grid sizes above 3.6 million cells.

The axial velocities were integrated to obtain total nominal wake fractions for each studied mesh, presented in Table 6.1 and Figure 6.10.

**Table 6.1 Results from the study**

Mesh	Nominal wake fraction	Refinement factor
15.2M	0.5327	0.77
7.4M	0.5250	1
3.6M	0.5105	1.3
1.8M	0.5008	1.69
0.9M	0.4861	2.22

**Figure 6.10** Wake fraction with respect to refinement ratio. Third order polynomial fit.

The results of the total nominal wake fraction do not show a clear convergence with more refined meshes, although the data is somewhat scattered. One possible reason for this is the higher  $y^+$  values produced by the less refined meshes. This is discussed further in Section 6.3.

## 6.2 Turbulence model comparison

For turbulence model comparison, three different version of  $k-\omega$  SST model were selected: standard  $k-\omega$  SST, curvature corrected with linear model and curvature corrected with cubic model. The 7.4M mesh was selected since there was a clear gap between predicted values of 3.6M mesh (Figure 6.6 and Figure 6.7), implying increased accuracy, and since it was computationally less heavy than 15.2M cell mesh.

The average  $y^+$  value in the simulation was approximately 0.8. The  $y^+$  values along the hull varied from about 0.2 to over 1. The distribution of values is visualized in Figure 6.11.



Figure 6.11 Values of  $y^+$  along the hull.

The velocity iso contours and wake fraction are presented in similar manner as in the previous section.

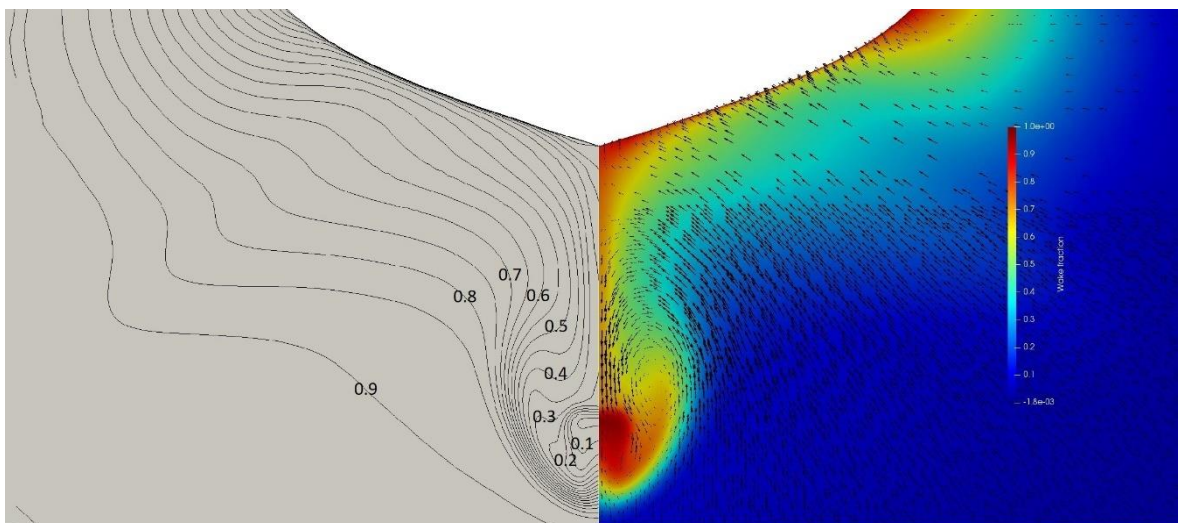


Figure 6.12 Axial velocity ratio iso-contours (left), wake fraction and transverse velocity vectors (right). 7.4M cells, standard SST  $k-\omega$ .

From Figure 6.12 it can be seen that the standard SST  $k-\omega$  turbulence model produces a noticeable, yet not very far reaching, bilge vortex.

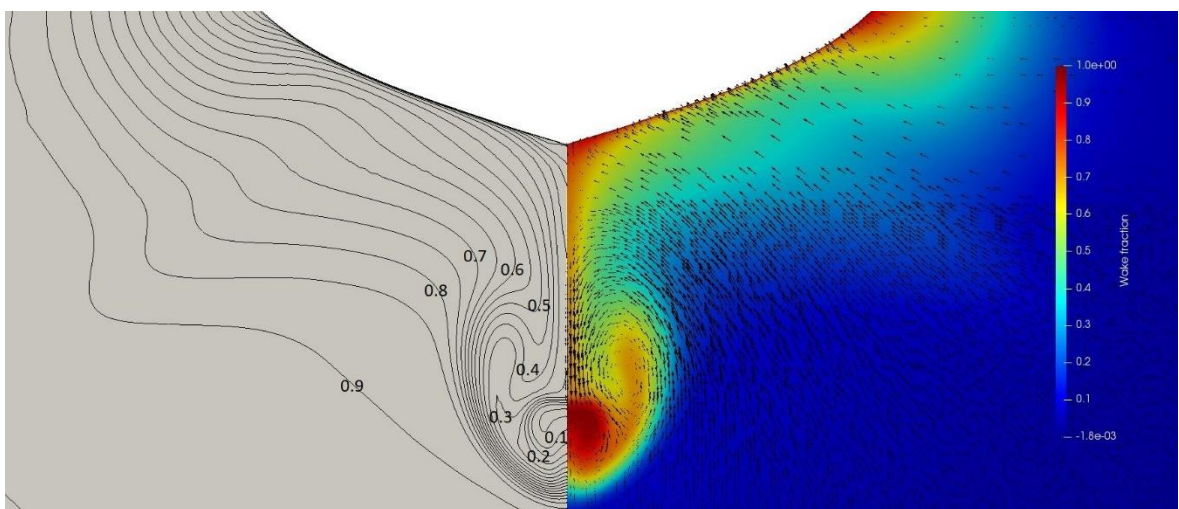
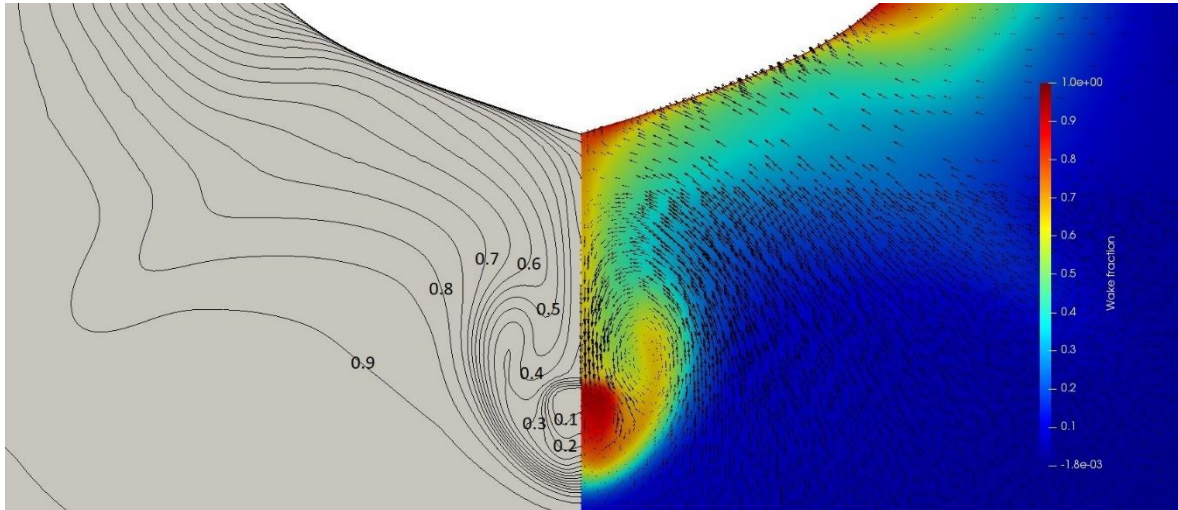


Figure 6.13 Axial velocity ratio iso-contours (left), wake fraction and transverse velocity vectors (right). 7.4M cells, curvature corrected SST  $k-\omega$ .

With the curvature corrected turbulence model shown in Figure 6.13, the hook shape of the bilge vortex is stronger and is spread out further at propeller radius than with standard SST  $k-\omega$  turbulence model of Figure 6.12.



**Figure 6.14** Axial velocity ratio iso-contours (left), wake fraction and transverse velocity vectors (right). 7.4M cells, curvature corrected cubic SST  $k-\omega$ .

In Figure 6.14, the bilge vortex is spread out further than with the linear curvature corrected turbulence model (Figure 6.13). The bilge vortex is slightly less intense when compared to the linear curvature corrected model.

Figure 6.15 (a) shows a plot similar to those of Figures 6.12-6.14, but with using data from towing tank tests. Comparing these figures, it is seen that the hook shape of bilge vortex is captured more accurately with both of the curvature-corrected turbulence models. However, in those curvature-corrected turbulence models, the intensity and location of the bilge vortex are different: the linear model predicts the location to be closer to the centerline than the cubic model does. Furthermore, the intensity of the bilge vortex differs between the linear and cubic models: the linear model predicts a more intense decrease in axial velocity in a smaller region, while the cubic model predicts the spreading of the low axial velocity area to be slightly less intense and further from the propeller hub. Results from the cubic model are shown in Figure 6.15 (b) for easy comparison to those from the towing tank tests.

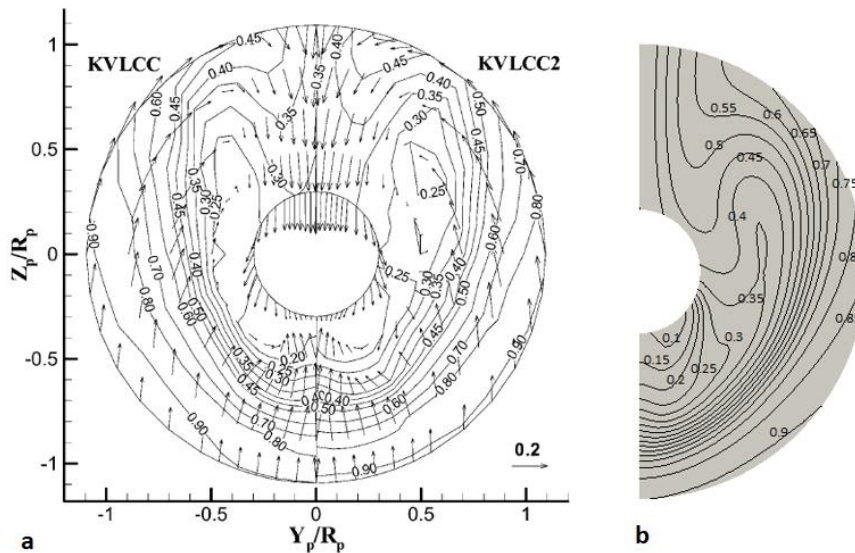


Figure 6.15 Left: measured wake distribution at the propeller plane of KVLCC and KVLCC2 (Kim et al., 2001). Right: results from the curvature corrected cubic turbulence model. The region plotted is that between 0.3 and 1.1 times the propeller radius.

There is noticeable similarity in the hook shape of the bilge vortex between the towing tank test and the simulation results. However, it is seen that curvature corrected cubic model underpredicts the intensity at the tip of the hook. For example, at the location in the towing tank test's hook tip where the wake fraction achieves a value of 0.25, the simulation gives an approximate wake fraction of 0.45. In general, the location of wake fraction iso-contours is shifted in the simulation: they appear uniformly lower at the propeller plane. As seen previously, similar characteristics are shown with linear curvature corrected model, although wake fraction is slightly smaller along the bilge vortex and the location of the vortex is shifted. Similarly to previous section, axial wake fractions are presented at four fractions of the propeller radius.

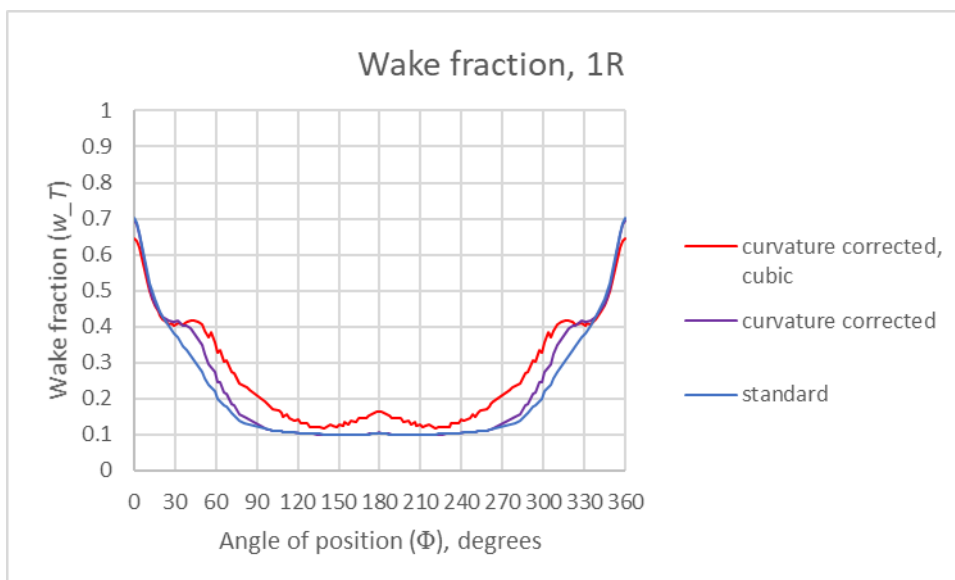
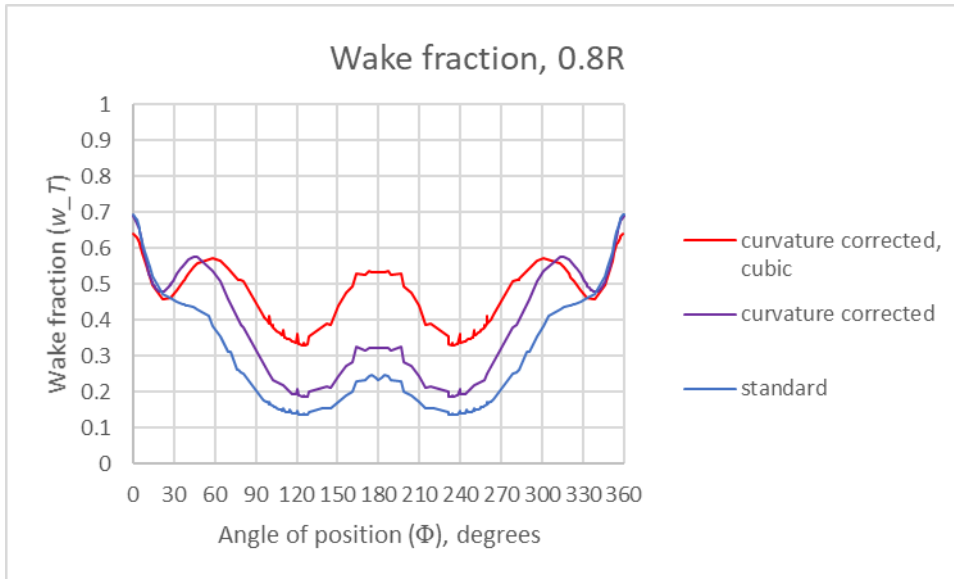


Figure 6.16 Axial wake fraction against peripheral angles, 1R.

As seen before, curvature corrected cubic SST  $k-\omega$  turbulence model predicts the wake fraction to be larger than in the other models from 40-320 degrees.



**Figure 6.17 Axial wake fraction against peripheral angles, 0.8R.**

At radius 0.8R, the different turbulence models show very different wake intensities. The difference grows towards the 180 degrees angle, where the curvature corrected cubic turbulence model predicts the wake fraction over two times the magnitude predicted by standard SST  $k-\omega$ .

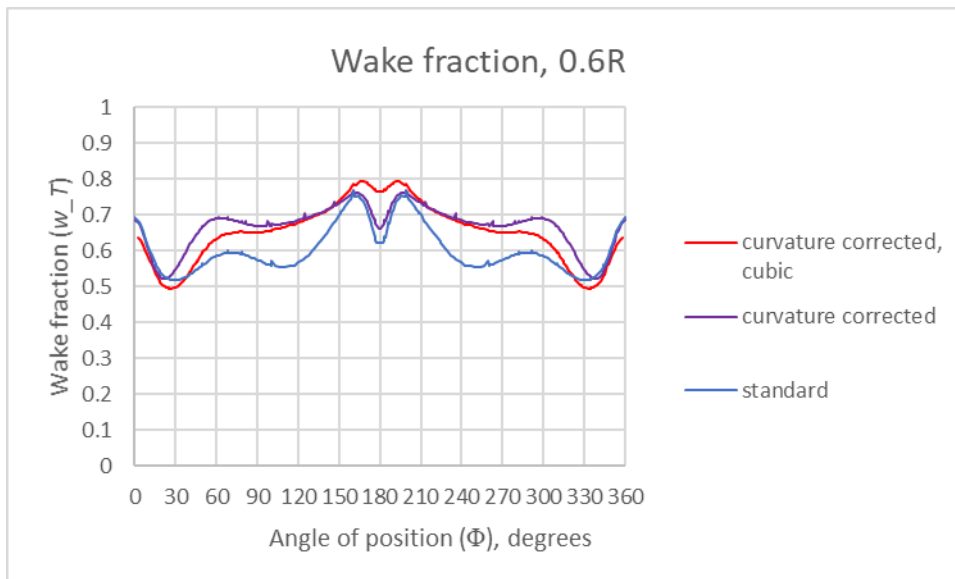


**Figure 6.18 Axial wake fraction against peripheral angles, 0.6R**

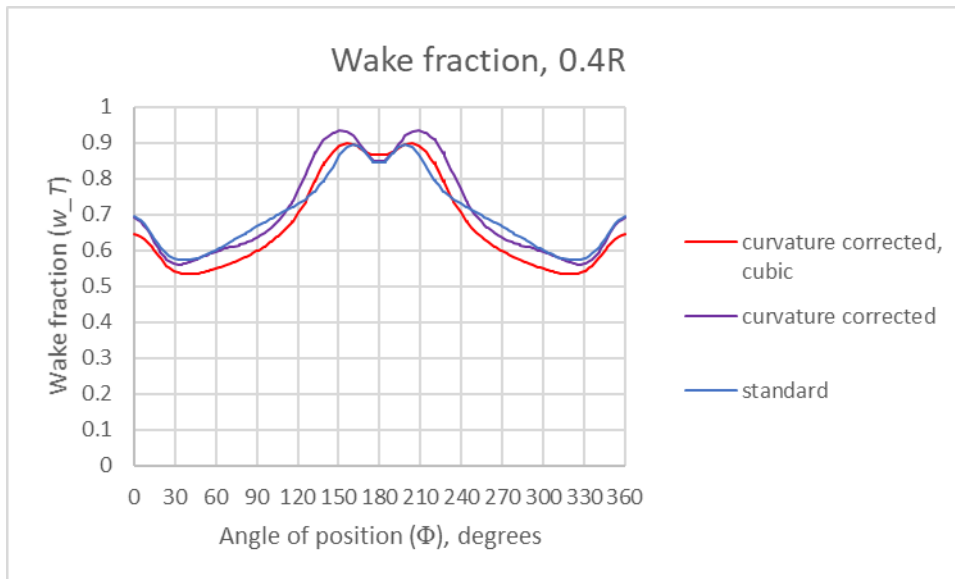


**Figure 6.19 Axial wake fraction against peripheral angles, 0.4R.**

It is seen from the Figure 6.18 and Figure 6.19 that curvature corrected turbulence models predict different intensities depending on location at the propeller plane: curvature corrected linear model predicts larger wake fraction at  $0.6R$  around 60 and 300 degrees while cubic model predicts more clearly more intense wake around 180 degrees position.

The axial velocities were integrated to obtain nominal wake fractions at propeller plane, Table 6.2. The nominal wake fraction varied greatly between the different turbulence models.

**Table 6.2 Nominal wake fraction at propeller plane**

Turbulence model	Nominal wake fraction
Standard SST $k-\omega$	0.4513
SST $k-\omega$ with curvature correction	0.4981
SST $k-\omega$ with curvature correction and cubic model	0.5250

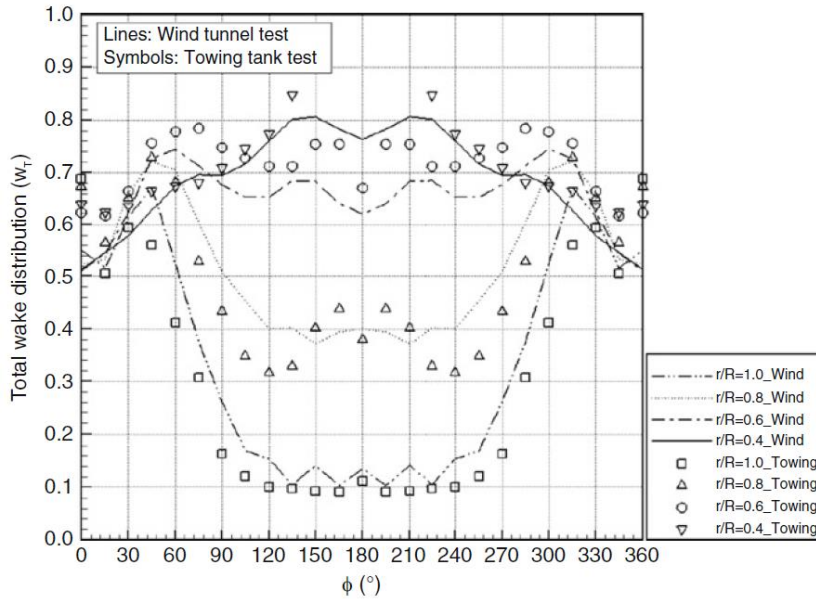


**Figure 6.20** Total wake fractions of KVLCC2 measured in wind tunnel by POSTECH (lines) and by KRISO (symbols) (Larsson et al., 2014). Note that here the notation  $w_T$  is used for the total wake distribution while in the rest of this thesis it is used for Taylor's wake fraction.

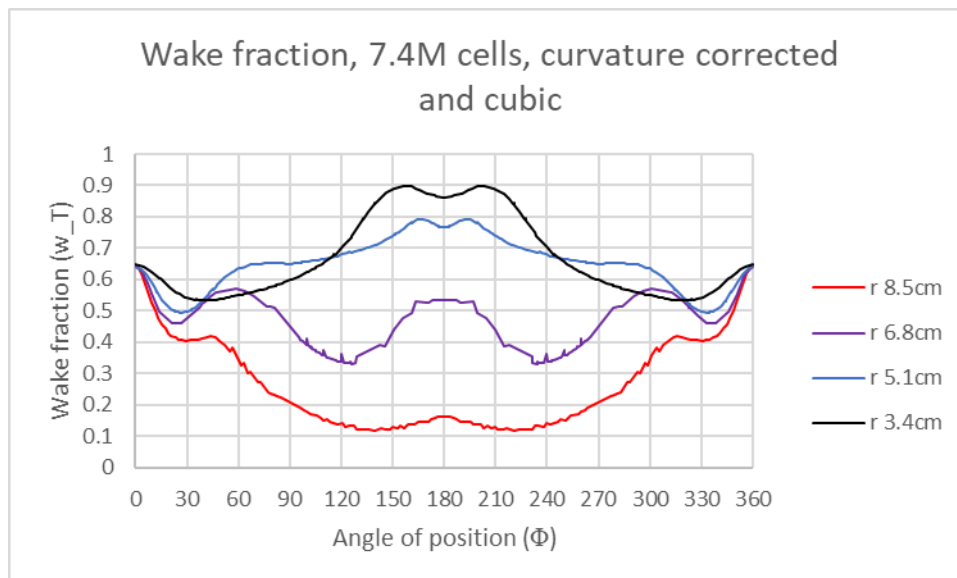


**Figure 6.21** Wake fraction of curvature corrected cubic model.

The radial wake fractions of the cubic model produce good predictions for wake peak locations compared to towing tank and wind tunnel test results (Figure 6.20). However, regarding the magnitude, wake peaks occurring at 60 degrees and correspondingly at 300 degrees in model tests are underpredicted. The wake peaks occurring at the upper end of propeller disk are overpredicted in the simulation and give wake fraction about 10-20% larger between 150 and 210 degrees. Similar results were achieved at the Gothenburg 2010 CFD workshop, where turbulence models predicted higher wake fractions especially at upper side of the propeller disk at  $0.8R$  and  $1R$  (Larsson et al., 2014). Gothenburg 2010 CFD workshop included a comparison between standard SST  $k-\omega$  and one with rotation correction, Figure 6.22.

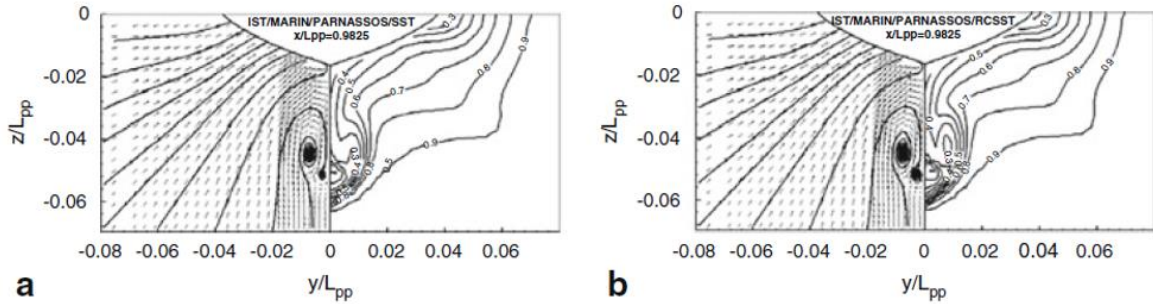


Figure 6.22 Difference between SST  $k-\omega$  and SST  $k-\omega$  with rotation correction. (Larsson et al., 2014)

The results from the curvature corrected turbulence model show a close similarity with the results obtained by IST-MARIN and presented at the Gothenburg 2010 Workshop, as shown in Figure 6.22b. The bilge vortex shape is very similar, although the values for wake fraction along the hook shape are generally smaller than the ones obtained in this case study. The differences between the standard and rotation corrected SST  $k-\omega$  turbulence models show similar characteristics as presented in this study.

### 6.3 Discussion

The results were mostly in line with previous research with the exception that no clear convergence of the results was achieved in grid convergence study. The results showed very similar characteristics to previous research with medium refined and most refined meshes, although the intensity of bilge vortex varied slightly.

The large differences in wake prediction occurred at  $0.6R$  and outwards. This is the region where standard SST  $k-\omega$  predicts significantly less intense bilge vortex. Linear and cubic models predict slightly different locations of the vortex: the wake on the upper region of propeller plane at  $0.6R$  is stronger with linear model while cubic model predicts it stronger at  $0.8R$  and outwards. Based on the results from the Gothenburg 2010 workshop, rotation corrected turbulence models tend to improve the predicted flow at the propeller plane, but flow upstream may not be in agreement with the experiments (Larsson et al., 2014).

It should be noted that since the grid was unstructured, grid refinement study had some variation in cell refinement because the number of cells within prismatic layer was set to even number. The grid structure has effect on the results. An example of this is given from the Tokyo 2015 CFD workshop in Figure 6.23, where the results from two teams using around 20 million cells and the same code are visualized. These simulations were conducted with free surface and taking on account sinkage and trim, unlike the ones in this thesis.

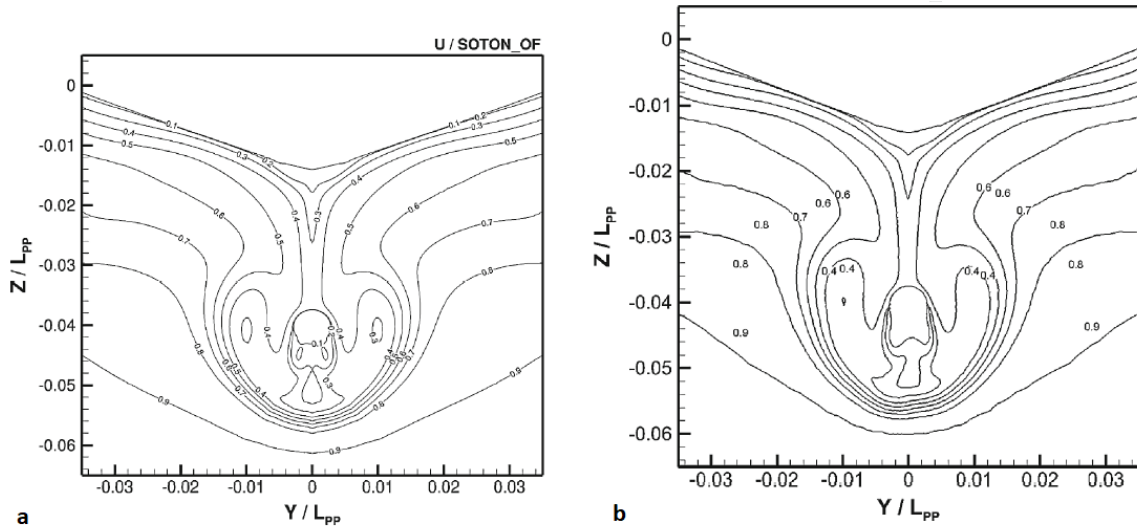


**Figure 6.23** Difference between wake predicted by two groups with similar grids of 20 million cells (a) and 25 million (b) cells with the same code. (Hino et al, 2021)

Although there are a lot of similarities in the predictions, shape of the bilge vortex varies noticeably between the studies. Intensities of the bilge vortex differ: in Figure 6.23 (a) the lower velocity zones inside the vortex tips are stronger and wider. Hino et al. (2021) mention that turbulence modeling error typically exceeds largely the discretization error with grids consisting of more than 2 million cells. Based on the results from the simulations and these findings, it was concluded that selection of the turbulence model has generally greater effect on the results than the used grid. Since there was still clear difference between the results predicted by 3.6M and 7.4M cells mesh, it can be assumed that wake field prediction can benefit from a mesh size of 5 million cells or more. However, it should be noted that the mesh refinement regions were likely not placed in the most efficient way, and that structured meshes could provide similar accuracy with lower number of grid points.

The wake was compared with Huse criteria. The maximum wake fraction above the shaft center line is high but does not exceed 0.7. Maximum acceptable wake peak criteria is satisfied, although the peak is high at the radius  $1R$ . Even though this satisfies the criteria, highly varying loads are caused but only at the tips of propeller blades. Wake peak around  $1R$  is high but the gap is wider than the distance between propeller blades. This could be a problem if the hook shape didn't extend so far at the propeller plane, since the peak would be narrower. Molland et al. (2011) mention that tangential wake decreases and increases loads on the blades during the rotation, thus inducing vertical loads on the shaft.

Kim et al. (2001) mention that the shape of KVLCC2 hull is designed for higher wake fraction than the previous test case model KVLCC. Even though the predicted resistance of KVLCC2 is larger than KVLCC2, Kim et al. (2001) mention that wake distribution of KVLCC2 hull gives higher quasi-propulsive efficiency. All in all, the wake distribution of KVLCC2 vessel could be made more favorable if the bilge vortex was more concentrated on the propeller without too high peaks and if tangential wake was reduced.

The computations were performed on a high-performance computing cluster. The simulations were divided into 16 processes which is in line with ITTC (2014b) recommendation of using 50 000 to 500 000 grid points per core, although this was exceeded with the finest

mesh with 15.2M cells. The processes were divided between 2-4 nodes depending on availability on the cluster. Elapsed time for simulation ranged from less than half an hour with the coarsest mesh to closer to 10 hours with the finest grid, although the mid-size grids are closer to practical range in ship design. Maximum memory of 6GB per process was reserved.

For example, for 7.4M cell grid with curvature corrected cubic turbulence model computation time was as follows. First, 3.6M cell mesh with curvature corrected model was run for 1 000 steps, using CPU (Central Processing Unit) time for 37 350 seconds. Then, the solution was mapped to 7.4M cell grid and run for another 1 000 steps, which used CPU time for 100 570 seconds. Total elapsed time was 8 646 seconds without taking on account time spent on mapping of the solution between the grids. Total simulation time was thus about two and half hours. Scalability of the simulation was efficient: CPU time per process was 8 621 seconds while elapsed time was 8 646 seconds, meaning that 99.7% efficiency was achieved.

It can be expected that modern performance workstations are capable of somewhat similar order of magnitude computing times, although memory requirements may set limitations to grid size. Since scaling of the simulation was so efficient, simulation could be divided between larger number of processes for faster computations without losing too much efficiency. Test runs would be needed to determine the actual scalability and performance of the used workstation. However, it can be noted that while using this amount of grid points, several iteration cycles for optimizing the hull form can be expected to take days rather than hours. For fast optimization cycles, it might be optimal to first run simulations with fewer grid points during active design time and then use more refined meshes for detailed comparison between efficient designs, practically between the workdays.

As seen in the grid refinement study, there was no clear convergence in wake fraction as the grid was refined. Based on findings from the study conducted by Eça et al., (2018), it was suspected that the reason for this could be the used cell thickness within prismatic layer, and that even smaller  $y^+$  values could be needed for more consistent results. Test cases were run with more refined prismatic layers to study the effect of this on the results, mostly using the curvature corrected cubic turbulence model. However, for the comparison between the 7.4M cell mesh and the modified mesh with a refined prismatic layer, the linear turbulence model was used instead, since convergence was not achieved with the cubic variant and the more refined mesh. The results are presented in Table 6.3.

**Table 6.3 Nominal wake fraction and friction coefficients from various simulations**

Mesh size	Average $y^+$	Turbulence model	Nominal wake fraction	$C_f(10^3)$
7.4M	0.8	curvature corrected, cubic	0.5250	3.14
7.4M	0.8	curvature corrected	0.4981	2.90
Refined prismatic layer mesh, 9M cells. Base mesh 7.4M.	0.12	curvature corrected	0.5156	3.05
3.6M	1.8	curvature corrected, cubic	0.5105	2.92
Refined prismatic layer mesh, 5M cells. Base mesh 3.6M.	0.12	curvature corrected, cubic	0.4934	3.07

The ITTC friction line gives an estimate of  $3.45 \cdot 10^{-3}$  for frictional resistance coefficient. Also, Eça et al. (2018) predict that results converge towards this when mesh is further refined (Figure 6.24). Results from the refined meshes studied in this thesis were roughly within the numerical uncertainties estimated by Eça et al. (2018), Figure 6.25.

Generally, curvature corrected cubic turbulence model and simulations with smaller  $y^+$  values predicted frictional resistance coefficients to be larger. Refined meshes predicted nominal wake fraction to be either larger (curvature corrected 7.4M cell mesh) or smaller (curvature corrected cubic 3.6M cell mesh) than with the original mesh. The reason for this may be high average  $y^+$  value of the original 3.6M cell mesh but no clear conclusions on the effect of wake fraction could be derived.

The frictional resistance coefficient results showed characteristics similar to the findings by Eça et al., (2018). In their research, Eça et al. studied the effect of grid refinement on frictional resistance coefficient of the KVLCC2 hull. The used meshes had 0.9 to 8.9 million cells and different  $y^+$  values for each set were used. The results from their studies are shown in Figure 6.24 and Figure 6.25.

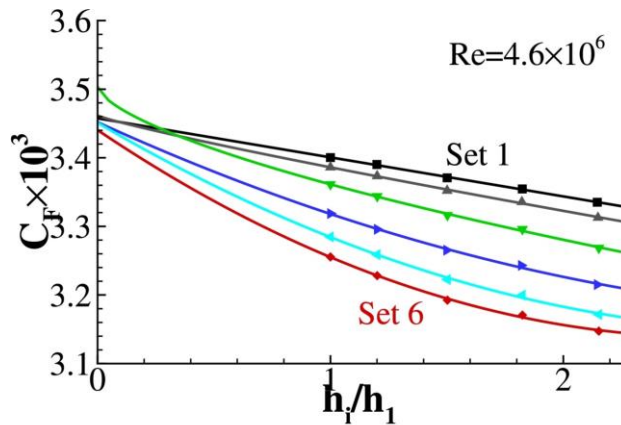


Figure 6.24 Friction resistance coefficients of the results with respect to grid refinement ratio. (Eça et al., 2018)

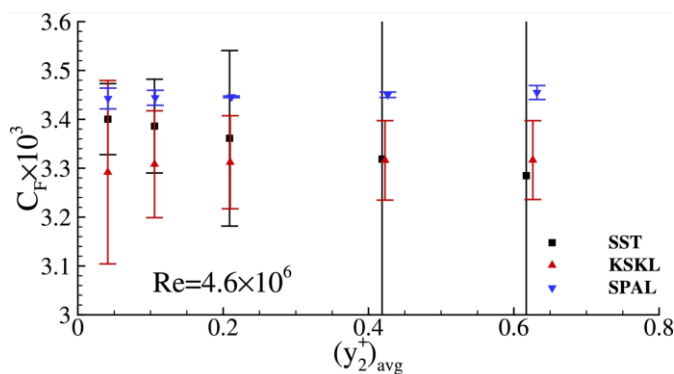


Figure 6.25 Friction resistance coefficients and their numerical uncertainties with respect to average near-wall cell size. (Eça et al., 2018)

It is seen from the Figure 6.25 that the numerical uncertainties when using SST  $k-\omega$  turbulence were significantly larger than with the other two turbulence models tested when the average near-wall cell size ( $(y_2^+)_{avg}$ ) was set larger than 0.4, corresponding to  $y^+$  values larger than 0.2. This likely affected the results of the grid convergence study in this thesis since the  $y^+$  values used were multiple times larger. Practically this means that the number of cells within the prismatic layer needs to be large and there may be convergence problems since the aspect ratios of the cells are high near the wall.

In addition to previously presented, an effort was made to build a full-scale simulation. However, the results achieved were not of the desired accuracy. There are various reasons this may have occurred. First, the aspect ratio of the prismatic layer cells grew very large. This occurred because computational resources prevented the generation of meshes with more than around 20M cells. Better results may have been achieved with a smaller spacing of prismatic layer cells, but this could not be tested. In addition, simulations tended to be unstable – convergence was only achieved with one of the generated meshes. However, even in this case the results were not of the desired quality, possibly due to overly large grid spacing. The mesh was made finer at the aft hull section, but the simulations with this modified mesh still did not converge despite numerous attempts.

## 7 Conclusions

In this thesis, two studies were conducted on model scale wake field of a KVLCC2 tanker. First, a refinement study was done on five meshes ranging from 0.9 to 15.2 million cells using curvature corrected cubic SST  $k-\omega$  turbulence model. Three different SST  $k-\omega$  turbulence models were then compared. The results were compared with both wind tunnel and towing tank tests, and with results from previously published CFD simulations. Wake fraction was overpredicted compared to results from towing tank tests. However, CFD simulation results from Gothenburg Workshop (Larsson et al., 2014) showed similar characteristics to the results achieved in this work.

With similar mesh refinement regions and turbulence models, there were still noticeable differences when the mesh was refined from 3.6 million to 7.4 million cells. This is somewhat in line with Gothenburg Workshop results with respect to grid size (Larsson et al., 2014), since accuracy seems to grow at a faster rate from 0.9 million to 3.6 million cells. Since Gothenburg Workshop error estimations were related to resistance prediction, and the sample size of simulations conducted with low Froude number vessels was small, the suggested grid size does not directly apply to wake field analysis. However, it can give an indication of the right size. Therefore, it can be concluded that for accurate predictions of model scale wake with a double body model, grids containing more than 5 million cells can improve the results.

It was generally observed that the chosen turbulence model had a larger impact on the results than mesh refinement. Both linear and cubic curvature corrected models predicted bilge vortex shape rather accurately but to be less intense than results from model tests. The intensity of the bilge vortex decreased with coarser grid resolution. Standard SST  $k-\omega$  turbulence model could not capture the bilge vortex shape accurately. This problem had been recognized in literature (ITTC, 2014a; Larsson et al., 2014) where rotation corrected SST  $k-\omega$  or other more advanced turbulence models were recommended. The current recommendations for  $y^+ < 1$  in near wall flow simulations (ITTC, 2014a) may be too high for the studied turbulence models. Similar conclusions have been made by Eça et al. (2018).

There are inaccuracies in scaling the wake from model to full scale. This could be avoided by simulating wake field directly in full scale. Full scale simulations were attempted in this study, but conducting the simulations was laborious with the used resources, and no satisfactory results were achieved. With different approaches in grid generation, such as by using structured grids, grid constructed of multiple blocks, or just by using larger number of cells, full scale simulations may be a viable option for wake prediction, especially when computational capabilities develop further.

There remains room for improvement in accuracy and reliability of the methods. Although current turbulence models can predict the characteristics of wake field rather accurately, towing tank tests are still conducted to get more reliable results (Bertram, 2012). This is not optimal for the design, since confident predictions on the vessel's hydrodynamic performance in early stages of design spiral would help to avoid mistakes in design.

The chosen turbulence model affects the results and although curvature/rotation corrected models may improve the results at wake field, the flow before the propeller plane is not so accurately predicted (Larsson et al., 2014). There was an indication that grids containing more than 5 million cells could improve the results, but this should be studied further. Better results in grid convergence study could be achieved by using structured grids in order to utilize the number of grid points more efficiently. The results achieved in the study using variations of SST  $k-\omega$  turbulence model seemed to be more dependent on the  $y^+$  values than what is commonly advised. The effect on refining the prismatic layer was briefly studied but more systematic approach should be used to get more insight on this.

## References

- Asén, P. (2014) *Analysis of the Flow Around a Cruise Ferry Hull by the Means of Computational Fluid Dynamics*. MA Diss, Espoo, Aalto University.
- Bertram, V. (2012) *Practical Ship Hydrodynamics (2nd Edition)*. Elsevier.
- Carlton, J. (2019) *Marine Propellers and Propulsion (4th Edition)*. Elsevier United Kingdom 2019. ISBN 978-0-08-100366-4
- Eça L., Pereira F., Vaz G. (2018) *Viscous flow simulations at high Reynolds numbers without wall functions: Is  $y^+ \approx 1$  enough for the near-wall cells?* Computers & Fluids, Vol. 170, pp. 157-175. DOI: 10.1016/j.compfluid.2018.04.035
- Esquivel de Pablo, P. (2013) *Analysis of the Shear Stress Distributions on Two Ship Hull Forms*. MA Diss, Espoo, Aalto University.
- Evans J. (1959) *Basic Design Concepts*. Journal of the American Society of Naval Engineers (ASNE), pp. 671–678. DOI: 10.1111/j.1559-3584.1959.tb01836.x
- Gale, P. (2003) *The Ship Design Process*. Presented in Ship Design and Construction, Volume 1. Society of Naval Architects and Marine Engineers (SNAME).
- Hansen H., Dinham-Peren, T. (2015) *Potential for Improvement of Ship Lifecycle Costs Through Deviation from Standard Ship Designs and Practices*. Presented in Energy Efficient Ships, 4<sup>th</sup> November 2015. RINA.
- Harvald, S. (1950) *Wake of Merchant Ships*. Danish Technical Press.
- Harvald, S. (1973) *Potential and Frictional Wake of Ships*. Transactions of the Royal Institution of Naval Architects, Vol. 115, 1973, pp. 315-325
- Hino T., Stern F., Larsson L., Visonneau M., Hirata N., Kim J. (Eds) (2021) *Numerical Ship Hydrodynamics. An Assessment of the Tokyo 2015 Workshop*. Springer International Publishing. DOI 10.1007/978-3-030-47572-7. Pre-published online in 2020.
- Huse, E. (1974) *Effect of Afterbody Forms and Afterbody Fins on the Wake Distribution of Single Screw Ships*. NSFJ Report No. R31-74.
- IMO. (2011) *RESOLUTION MEPC.203(62)*. IMO.
- IMO. (2020) *Energy Efficiency Measures*. IMO. Viewed 14.7.2020. <<http://www.imo.org/en/OurWork/Environment/PollutionPrevention/AirPollution/Pages/Technical-and-Operational-Measures.aspx>>

- ITTC. (1957) *Skin Friction and Turbulence Stimulation*. International Towing Tank Conference 1957.
- ITTC. (2011) *Recommended Procedures and Guidelines – The Specialist Committee on Scaling of Wake Field*. The Specialist Committee on Scaling of Wake Field of the 26<sup>th</sup> ITTC.
- ITTC. (2014a) *Recommended Procedures and Guidelines – Practical Guidelines for RANS Calculation of Nominal Wakes*. Specialist Committee on CFD in Marine Hydrodynamics of the 27<sup>th</sup> ITTC.
- ITTC. (2014b) *Recommended Procedures and Guidelines – Practical Guidelines for Ship CFD applications*. Specialist Committee on CFD in Marine Hydrodynamics of the 26<sup>th</sup> ITTC.
- Kim, W., Van, S. & Kim, D. (2001) *Measurement of flows around modern commercial ship models*. Experiments in Fluids 31, pp. 567–578. DOI: 10.1007/s003480100332
- Kundu, P. & Cohen, I. (2008) *Fluid Mechanics. 4th ed.* Academic Press, Amsterdam, Netherlands.
- Larsson L., Stern F., Visonneau, M. (Eds) (2014) *Numerical Ship Hydrodynamics – An assessment of the Gothenburg 2010 Workshop*. Springer, Dordrecht, Netherlands. ISBN 978-94-007-7189-5
- Larsson L., Raven H. (2010) *Principles of Naval Architecture Series - Ship Resistance and Flow. Society of Naval Architects and Marine Engineers (SNAME)*.
- Maersk. (2020) *Case studies. Progress 2019: Help to Decarbonise Logistics*. Viewed 14 November 2020. < <https://www.maersk.com/news/articles/2020/02/20/progress-2019-help-to-decarbonise-logistics>>
- Molland A., Turnock S., Hudson D. (2011). *Ship Resistance and Propulsion - Practical Estimation of Ship Propulsive Power*. Cambridge University Press.
- Nishikawa et al. (2012). *Application of Fully-resolved Large Eddy Simulation to KVLCC2*. Journal of the Japan Society of Naval Architects and Ocean Engineers. Vol. 16, pp. 1-9. DOI: 10.2534/jjasnaoe.16.1
- Odabasi A., Fitzsimmons P. (1978) *Alternative Methods for Wake Quality Assessment*. Int. ShipBuild. Prog. 25 (282).
- Papanikolaou, A. (Ed) (2019) *A Holistic Approach to Ship Design*. Springer Nature Switzerland. ISBN 978-3-030-02809-1

Polezhayeva H., Norwood M., Ward T. (2011) *Tanker Hull Structure Cracks: Costs, Benefits of Prevention, Framework for Management and Remedy*. Presented at RINA International Conference on Design and Operation of Tankers. ISBN 978-1-905040-85-8

SIMMAN 2008. (2008) *MOERI Tanker KVLCC2. Geometry and Conditions*. Viewed 9.3.2020. <[http://www.simman2008.dk/KVLCC/KVLCC2/kvlcc2\\_geometry.html](http://www.simman2008.dk/KVLCC/KVLCC2/kvlcc2_geometry.html)>

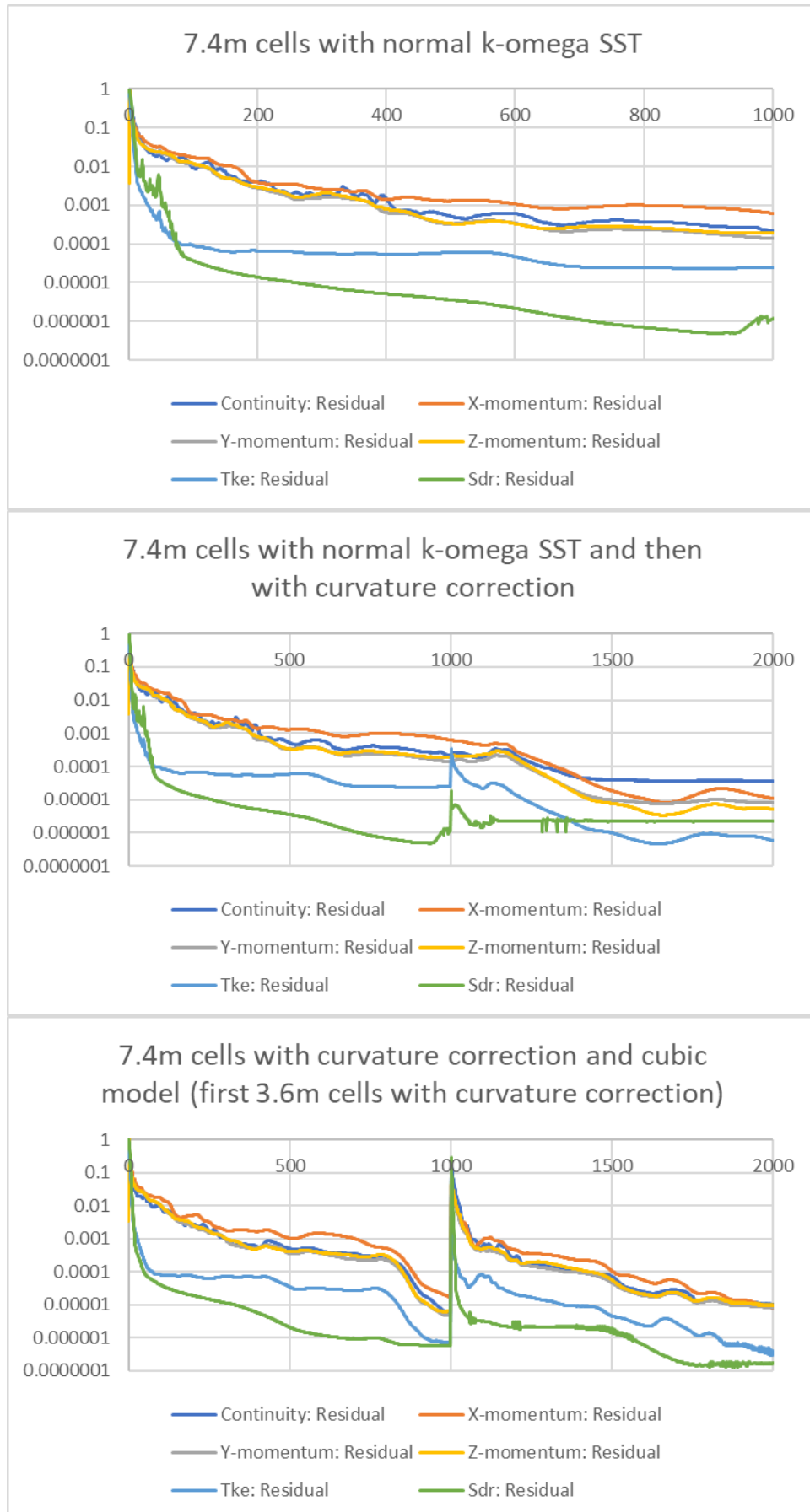
Schoenherr, K. (1932) *Resistance of Flat Surfaces Moving Through Fluid*. Trans. SNAME, Vol. 40, 1932.

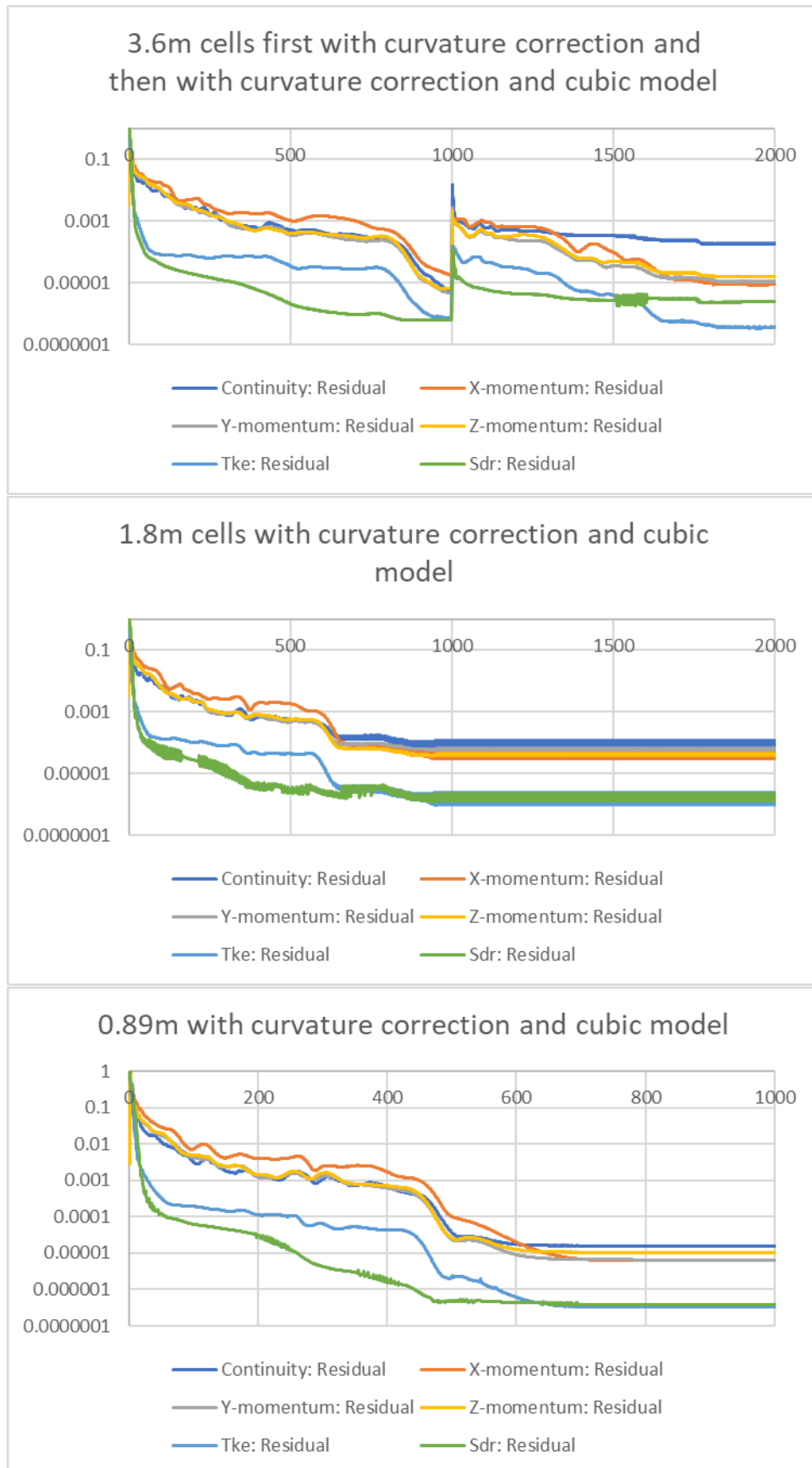
Schlichting, H. (1987). *Boundary Layer Theory* (7<sup>th</sup> ed.). New York, NY: McGraw-Hill.

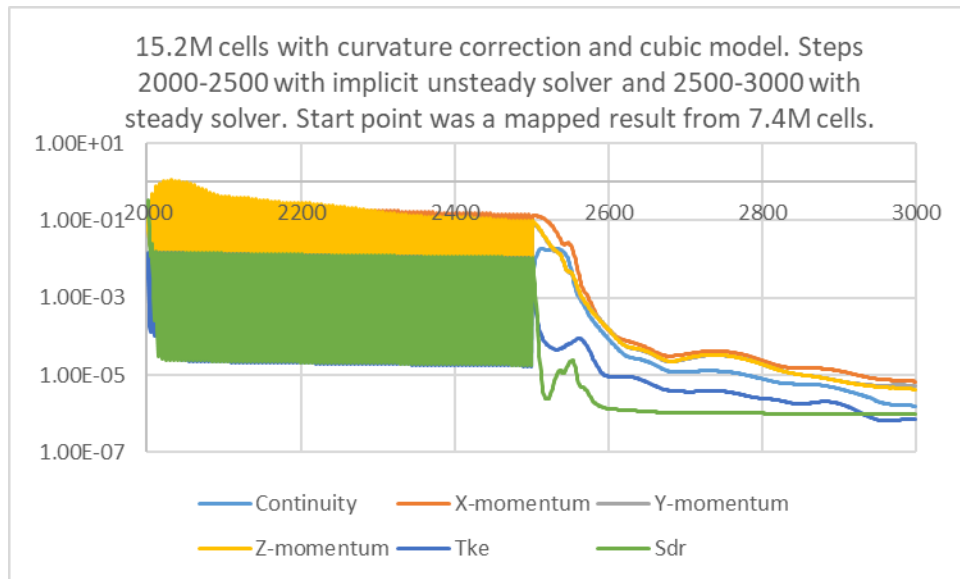
van Gunsteren, L., Pronk, C. (1973) *Propeller Design Concepts*. Int. Shipbuild. Prog. 20 (227).

## **The List of Appendices**

- Annex 1. Residual plots
- Annex 2. StarCCM+ files









11/21/2020

35msorig136@02000

```

    | | | ^-2 Dynamic Viscosity
    | | | ^-1 Constant
    | | | +-7 Reynolds-Averaged Navier-
Stokes | | |
    | | | +-8 Segregated Flow
    | | |
    | | |
    | | | +-9 Solution Interpolation
    | | |
    | | | +-10 SST (Menter) K-Omega
    | | |
    | | |
    | | | +-1 Compressibility Parameters
    | | | +-2 Realizability Coefficient
    | | | ^-3 Curvature Correction
Parameters | | |
    | | |
    | | | +-11 Steady
    | | | +-12 Three Dimensional
    | | | +-13 Turbulent
    | | | ^-14 Wall Distance
    | | | +-2 Reference Values
    | | | +-1 Gravity
    | | | +-2 Reference Altitude
    | | | +-3 Minimum Allowable Wall
Distance | | |
    | | | +-4 Maximum Allowable Absolute
Pressure | | |
    | | | +-5 Minimum Allowable Absolute
Pressure | | |
    | | | ^-6 Reference Pressure
    | | | ^-3 Initial Conditions
    | | | +-1 Pressure
    | | | | ^-1 Constant
    | | | +-2 Turbulence Intensity
    | | | | ^-1 Constant
    | | | +-3 Turbulence Specification
    
```

Method	Constant
Value	8.8871E-4 Pa-s

Positivity Rate Limit	0.2
Flow Boundary Diffusion	true
Unsteady Flux Dissipation Corrections	false
Limit Acoustic-CFL Option	Per-Model
Secondary Gradients	On
Convection	2nd-order
Delta-V Dissipation	Off
Per Part Mapping	false
Interpolation Method	Nearest neighbor
Legacy Method	false
Conservation Correction	Disable
Curvature Correction Option	On
Realizability Option	Durbin Scale Limiter
Compressibility Correction	true
Low Re Damping Modification	false
Convection	2nd-order
Normal Stress Term	false
Tke Minimum	1.0E-10
Sdr Minimum	1.0E-10
Secondary Gradients	On
Kappa	0.41
BetaStar	0.09
Beta1	0.075
Sigma_k1	0.85
Sigma_w1	0.5
Beta2	0.0828
Sigma_k2	1.0
Sigma_w2	0.856
Constitutive Option	Cubic
a1	0.31
Zeta_Star	1.5
Realizability Coefficient	0.6
Cr1	0.04645
Cr2	0.25
Cct	2.0
Upper Limit	1.25
Continuum Iteration	2000

Wall Distance Method	Implicit Tree
----------------------	---------------

Value	[0.0, 0.0, -9.81] m/s^2
Value	[0.0, 0.0, 0.0] m
Value	1.0E-6 m

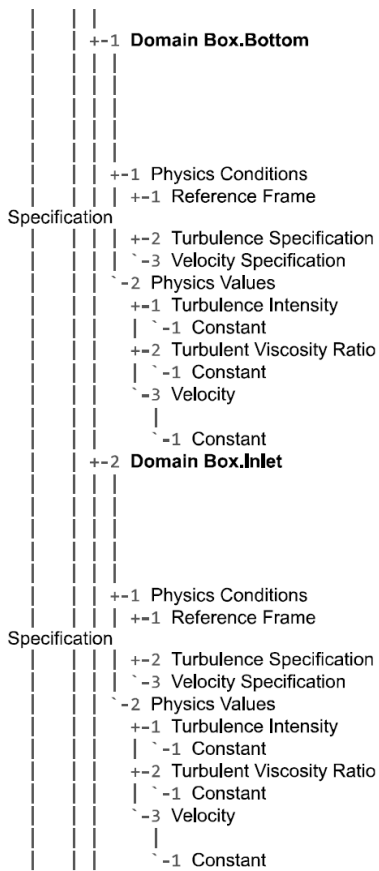
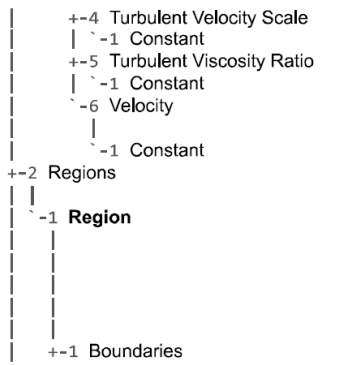
Value	1.0E8 Pa
-------	----------

Value	1000.0 Pa
-------	-----------

Value	101325.0 Pa
-------	-------------

Method	Constant
Value	0.0 Pa
Method	Constant
Value	0.01
Method	Intensity + Viscosity Ratio

11/21/2020



file:///Y:/triton73mfinalcurcub/summary of final curcub.html

35msorig136@02000

Method	Constant
Value	1.0 m/s
Method	Constant
Value	10.0
Method	Constant
Coordinate System	Laboratory
Value	[-1.047, 0.0, 0.0] m/s
Part Selection Priority	[Region]
Regions	1
Index	0
Physics Continuum	Physics 1
Parts	[]
Type	Fluid Region
Allow Per-Part Values	false
Tags	[]
Part Surface Selection Priority	[Region: kvlcc2fsfixed3,kvlcc2fsfixed3, Region: kvlcc2fsfixed3,kvlcc2fsfixed3 2, Region: Domain Box,Outlet, Region: Symmetry, Region: Domain Box,Bottom, Region: Domain Box,Top, Region: Domain Box,Port, Region: Domain Box.Inlet]
Boundaries	8
Index	5
Interfaces	
Part Surfaces	[]
Type	Velocity Inlet
Allow Per-Surface Values	false
Tags	[]

Option	Lab Frame
Method	Intensity + Viscosity Ratio
Method	Components

Method	Constant
Value	0,01
Method	Constant
Value	10,0
Method	Constant
Coordinate System	Laboratory
Value	[-1,047, 0,0, 0,0] m/s
Index	8
Interfaces	
Part Surfaces	[]
Type	Velocity Inlet
Allow Per-Surface Values	false
Tags	[]

Option	Lab Frame
Method	Intensity + Viscosity Ratio
Method	Components

Method	Constant
Value	0,01
Method	Constant
Value	10,0
Method	Constant
Coordinate System	Laboratory
Value	[-1,047, 0,0, 0,0] m/s

11/21/2020

35msorig136@02000

		+-3	<b>Domain Box.Outlet</b>
		+-1	Physics Conditions
			+-1 Backflow Specification
		+-2	Pressure Outlet Option
		+-3	Reference Frame
Specification			
		^-4	Turbulence Specification
		-2	Physics Values
		+-1	Pressure
			^-1 Constant
		+-2	Turbulence Intensity
			^-1 Constant
		^-3	Turbulent Viscosity Ratio
			^-1 Constant
		+-4	<b>Domain Box.Port</b>
		+-1	Physics Conditions
		+-1	Reference Frame
Specification			
		+-2	Turbulence Specification
		^-3	Velocity Specification
		-2	Physics Values
		+-1	Turbulence Intensity
			^-1 Constant
		+-2	Turbulent Viscosity Ratio
			^-1 Constant
		^-3	Velocity
			^-1 Constant
		+-5	<b>Domain Box.Top</b>
		+-6	<b>kvlcc2fsfixed3.kvlcc2fsfixed3</b>
		+-1	Physics Conditions
		+-1	Reference Frame
Specification			
		+-2	Shear Stress Specification
		+-3	Tangential Velocity
Specification			
		^-4	Wall Surface Specification
		-2	Physics Values
			^-1 Blended Wall Function

Index	3
Interfaces	
Part Surfaces	[]
Type	Pressure Outlet
Allow Per-Surface Values	false
Tags	[]
Direction	Boundary-Normal
Pressure	Environmental
Scalars	Specified
Option	None
Option	Lab Frame
Method	Intensity + Viscosity Ratio
Method	Constant
Value	0,0 Pa
Method	Constant
Value	0,01
Method	Constant
Value	10,0
Index	7
Interfaces	
Part Surfaces	[]
Type	Velocity Inlet
Allow Per-Surface Values	false
Tags	[]
Option	Lab Frame
Method	Intensity + Viscosity Ratio
Method	Components
Method	Constant
Value	0,01
Method	Constant
Value	10,0
Method	Constant
Coordinate System	Laboratory
Value	[-1,047, 0,0, 0,0] m/s
Index	6
Interfaces	
Part Surfaces	[]
Type	Symmetry Plane
Allow Per-Surface Values	false
Tags	[]
Index	1
Interfaces	
Part Surfaces	[]
Type	Wall
Allow Per-Surface Values	false
Tags	[]
Option	Region Reference Frame
Method	No-Slip
Method	Fixed
Method	Smooth
E	9,0

11/21/2020

35msorig136@02000

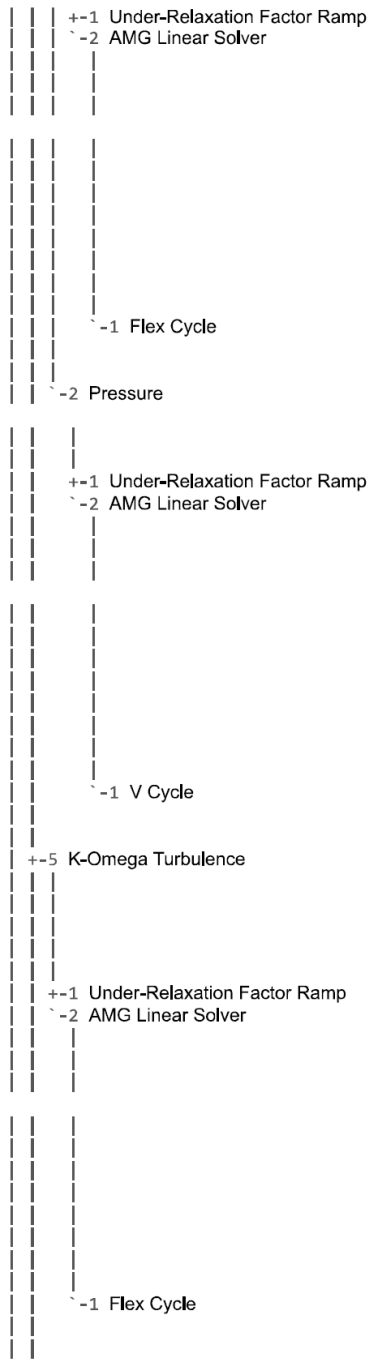
- +-7 kvlcc2fsfixed3.kvlcc2fsfixed3 2
  - +-1 Physics Conditions
    - +-1 Reference Frame
      - +-2 Shear Stress Specification
      - +-3 Tangential Velocity
    - +-4 Wall Surface Specification
      - 2 Physics Values
        - 1 Blended Wall Function
    - 8 Symmetry
      - +-2 Physics Conditions
        - +-1 Initial Condition Option
        - +-2 Mass Source Option
        - +-3 Momentum Source Option
        - 4 Turbulence Source Option
      - 3 Physics Values
        - +-1 Axis
        - 2 Motion Specification
- +-3 Representations
  - 1 Volume Mesh
    - +-1 Finite Volume Regions
      - 1 Region
        - 1 Finite Volume Boundaries
          - +-1 Domain Box, Bottom
          - +-2 Domain Box, Inlet
          - +-3 Domain Box, Outlet
          - +-4 Domain Box, Port
          - +-5 Domain Box, Top
          - +-6 kvlcc2fsfixed3.kvlcc2fsfixed3
          - +-7 kvlcc2fsfixed3.kvlcc2fsfixed3
        - 8 Symmetry
      - 2 Cell Sets
  - +-4 Contacts
  - +-5 Parts
  - +-6 3D-CAD Models
  - +-7 Coordinate Systems
    - 1 Laboratory
      - 1 Local Coordinate Systems
  - +-8 Tables

Kappa	0.42
Index	2
Interfaces	
Part Surfaces	[]
Type	Wall
Allow Per-Surface Values	false
Tags	[]
Option	Region Reference Frame
Method	No-Slip
Method	Fixed
Method	Smooth
E	9.0
Kappa	0.42
Index	4
Interfaces	
Part Surfaces	[]
Type	Symmetry Plane
Allow Per-Surface Values	false
Tags	[]
Option	Use Continuum Values
Mass Source Option	false
Momentum Source Option	None
Turbulence Source Option	None
Coordinate System	Laboratory
Origin	[0.0, 0.0, 0.0] m
Direction	[0.0, 0.0, 1.0]
Motion	Stationary
Reference Frame	Lab Reference Frame
Cells	7365047
Interior Faces	21752284
Vertices	7336568
Tags	[]
Cells	7365047
Interior Faces	21752284
Vertices	7336568
Edges	0
Faces	283
Faces	76
Faces	202
Faces	283
Faces	66780
Faces	195692
Faces	525
Faces	66204
Tags	[]



11/21/2020

35msorig136@02000



Ramp Method	No Ramp
Max Cycles	30
Verbosity	NONE
Enable Direct Solver	false
Maximum Direct Solver	32
Equations	
Convergence Tolerance	0.1
Epsilon	0.0
Cycle Type	Flex Cycle
Group Size Control	Auto
Group Size	4
Relaxation Scheme	Gauss-Seidel
Acceleration Method	None
Scaling	Disabled
Restriction Tolerance	0.9
Prolongation Tolerance	0.5
Sweeps	1
Number of Non-Orthogonality	0
Correctors	
Under-Relaxation Factor	0.3
Pressure Reference Location	Automatic Selection
Ramp Method	No Ramp
Max Cycles	30
Verbosity	NONE
Enable Direct Solver	false
Maximum Direct Solver	32
Equations	
Convergence Tolerance	0.1
Epsilon	0.0
Cycle Type	V Cycle
Group Size Control	Auto
Group Size	4
Relaxation Scheme	Gauss-Seidel
Acceleration Method	Conjugate Gradient
Scaling	Auto
Pre-Sweeps	1
Post-Sweeps	1
Max Levels	50
Solver Frozen	false
Reconstruction Frozen	false
Reconstruction Zeroed	false
Temporary Storage Retained	false
Under-Relaxation Factor	0.8
Boundary Layer Initialization	false
Ramp Method	No Ramp
Max Cycles	30
Verbosity	NONE
Enable Direct Solver	false
Maximum Direct Solver	32
Equations	
Convergence Tolerance	0.1
Epsilon	0.0
Cycle Type	Flex Cycle
Group Size Control	Auto
Group Size	4
Relaxation Scheme	Gauss-Seidel
Acceleration Method	None
Scaling	Disabled
Restriction Tolerance	0.9
Prolongation Tolerance	0.5
Sweeps	1

11/21/2020

`-6 K-Omega Turbulent Viscosity

+-32 Stopping Criteria

+1 **Maximum Steps**-2 **Stop File**

+-33 Solution Histories

+-34 Solution Views

-1 **Current Solution**

+-35 Layout Views

35msorig136@02000

Solver Frozen	false
Under-Relaxation Factor	1.0
Maximum Ratio	100000.0
Verbose	false
Enabled	true
Maximum Steps	2000
Logical Rule	Or
Criterion Satisfied	true
Tags	[]
Enabled	true
Stop Inner Iterations	true
Path	ABORT
Logical Rule	Or
Criterion Satisfied	false
Tags	[]

Iteration	2000
Time Step	0
Solution Time	0.0
Tags	[]

**Solution**

Accumulated CPU Time over all processes (s) 100570.46999999907  
 Elapsed Time (s) 6305.399728594348  
 Iterations 2000